OUT-OF-DISTRIBUTION GENERALIZATION OF DEEP-LEARNING SURROGATES FOR 2D PDE-GENERATED DYNAMICS IN THE SMALL-DATA REGIME

Binh Duong Nguyen *
Institute for Advanced Simulations – Materials Data Science and Informatics (IAS-9),
Forschungszentrum Jülich GmbH,
Jülich 52425, Germany

Stefan Sandfeld *
Institute for Advanced Simulations – Materials Data Science and Informatics (IAS-9),
Forschungszentrum Jülich GmbH,
Jülich 52425, Germany
Chair of Materials Data Science and Materials Informatics,
Faculty 5 – Georesources and Materials Engineering,
RWTH Aachen University,
Aachen 52056, Germany

ABSTRACT

Partial differential equations (PDEs) are a central tool for modeling the dynamics of physical, engineering, and materials systems, but high-fidelity simulations are often computationally expensive. At the same time, many scientific applications can be viewed as the evolution of spatially distributed fields, making data-driven forecasting of such fields a core task in scientific machine learning. In this work we study autoregressive deep-learning surrogates for two-dimensional PDE dynamics on periodic domains, focusing on generalization to out-of-distribution initial conditions within a fixed PDE and parameter regime and on strict small-data settings with at most $\mathcal{O}(10^2)$ simulated trajectories per system. We introduce a multi-channel U-Net with enforced periodic padding (me-UNet) that takes short sequences of past solution fields of a single representative scalar variable as input and predicts the next time increment. We evaluate me-UNet on various PDE families and compare it to ViT, AFNO, PDE- Transformer, and KAN-UNet under a common training setup. Across all datasets, me-UNet matches or outperforms these more complex architectures in terms of field- space error, spectral similarity, and physics-based metrics for in-distribution rollouts, while requiring substantially less training time, and also generalizes qualitatively to unseen initial conditions.

1 INTRODUCTION

Scientific and engineering practice increasingly relies on numerical models and data-driven methods to understand, predict, and control complex dynamical systems. Many such systems can be viewed as the evolution of spatially distributed fields over time and space. A central goal of scientific machine learning (SCIML) (Dietrich & Schilders, 2025) is therefore to learn such field dynamics from data, either in a purely data-driven fashion or by additionally exploiting assumed or derived governing equations, for example by integrating scientific knowledge with machine learning as discussed in recent surveys such as (Willard et al., 2023).

The behavior of any real systems is extremely complex with a large number of unknown parameters and relations. Therefore, in practice, idealized mathematical models expressed as systems of equations are used as a substitute. For a large class of phenomena, these equations take the form

*Corresponding author: bi.nguyen@fz-juelich.de, s.sandfeld@fz-juelich.de

of partial differential equations (PDEs), which encode, e.g., local conservation laws, balance relations, and constitutive assumptions. PDE models underpin applications from general relativity and quantum mechanics to fluid dynamics, elasticity, reaction–diffusion, and continuum descriptions in materials science. Examples of famous PDEs include Einstein's equations of general relativity (Einstein, 1915), the Schrödinger equation (Schrödinger, 1926) for the evolution of quantum-mechanical wave functions, and the Navier–Stokes equations (Navier, 1821) governing the motion of viscous fluids. Their flexibility and reach make PDEs some of the most widely used tools for representing spatio-temporal field evolution in science and engineering, even though they always remain idealized approximations of reality. The particular choice of PDEs determines which classes of phenomena can be represented, and the broad variety of PDEs models reflects the breadth of field dynamics encountered in practice.

When high-fidelity PDE models are available, they play a dual role in SCIML. First, they are scientifically important in their own right: many PDEs of interest are challenging to solve numerically, and accurate simulations can require substantial computational resources (Vogelsberger et al., 2014; Randall et al., 2019). Second, PDE solvers provide a controlled and reproducible way to generate training data with known ground truth. By sampling initial and boundary conditions, various parameters, and forcing terms, one can construct benchmark datasets that probe a range of dynamical regimes while avoiding experimental noise, measurement artifacts, and uncertainty about the underlying equations. In this sense, PDE-based benchmarks are an attractive stepping stone towards the much harder problem of learning from real measurement data, where the governing equations may be only partially known or not explicitly available. Here we instead emphasize strict small-data regimes, periodic 2D dynamics, and physics-based evaluation, aiming to mimic the constraints of many real scientific applications where generating each high-fidelity simulation is expensive.

From this perspective, PDEs in our work are not an end in themselves but a convenient and stringent testbed for models that aim to learn complex field dynamics. A SCIML method that fails to robustly learn dynamics generated by well-posed PDEs—in a setting where the discretization, parameters, and numerical errors are under control—is unlikely to succeed on heterogeneous, noisy, and partially observed real-world data. Conversely, architectures that generalize well across PDE-generated datasets, in particular under limited-data and out-of-distribution (OOD) conditions, are promising candidates for deployment on experimental or observational datasets. Thus, our choice to study 2D PDE dynamics is motivated both by the intrinsic importance of PDEs in science and engineering and by their role as a controlled proxy for more complex real-world field evolution.

Deep learning (DL) surrogates fit naturally into this program. Once trained, such surrogates can produce approximate multi-step forecasts at drastically reduced inference cost compared to conventional solvers, enabling tasks such as accelerated parameter studies, uncertainty quantification, or real-time control. We refer to a sequence of such predicted future fields, obtained by iteratively applying the learned time-advance operator starting from a ground-truth context, as an *autoregressive rollout*. However, real scientific applications typically operate in *small-data regimes*, where only tens to hundreds of high-fidelity simulations or experiments are available, and where test conditions may differ markedly from those seen during training. In this regime, the central challenge is not merely to fit a training distribution, but to achieve qualitatively robust, moderately OOD generalization of field dynamics while keeping training costs within the reach of typical scientific users.

A large body of work has explored neural networks as surrogates for differential equations. Early approaches in the 1990s already exploited universal approximation results for feed-forward networks (Hornik et al., 1989) to represent solutions of ordinary and partial differential equations in collocation schemes, e.g. as in (Lee & Kang, 1990; Dissanayake & Phan-Thien, 1994; Lagaris et al., 1998). More recently, several influential lines of research have emerged such as Fourier Neural Operator (FNO) (Li et al., 2020), Deep Operator Networks (DEEPONETS) (Lu et al., 2021), Physics-Informed Neural Networks (PINNs) (Raissi et al., 2019; Zhu et al., 2019; Shukla et al., 2020; Zhang et al., 2020; Ren et al., 2022; 2023; Yuan et al., 2024), and most recently, foundation-style PDE models (Sun et al., 2025; Holzschuh et al., 2025). Despite these advances, comparatively little work systematically investigates how relatively simple, carefully designed convolutional architectures perform as time-stepping surrogates for 2D field dynamics under strict small-data constraints and OOD initial conditions.

In this work, we adopt the latter viewpoint and use PDE-generated field dynamics as a controlled testbed for studying OOD generalization of DL surrogates in realistic small-data regimes. Con-

cretely, we consider two-dimensional, periodic field dynamics generated by five qualitatively different PDE families that cover transport, diffusion, pattern formation, and microstructure evolution. We then ask how different architectures behave when trained on at most a few dozen to one hundred simulations per PDE, and evaluated both on held-out simulations from the same distribution and on initial conditions that differ substantially from those seen during training. Our focus is on autoregressive surrogates that operate as time-stepping models, taking short sequences of past solution fields as input and predicting the next temporal increment, and on how architectural inductive biases (such as convolutional locality and periodic padding) influence data efficiency and out-of-distribution behavior. Our results highlight that, in small-data, periodic 2D field-dynamics settings, carefully designed convolutional baselines remain strong contenders for accurate and moderately out-of-distribution-robust surrogate modeling. More broadly, our study underscores the importance of evaluating SciML architectures under realistic data constraints and physics-aware metrics, and supports the use of PDE-generated benchmarks as a rigorous stepping stone toward models that can robustly learn from real experimental and observational data.

2 Mathematical model and neural network architecture

2.1 Mathematical model

In this work we consider six mathematical models of increasing complexity, listed in Tab. 1. They differ not only in the type of dynamics (transport, diffusion, pattern formation, turbulence, microstructure evolution) but also in the number and coupling of state variables. We organize them into three groups: single-field linear transport and diffusion (PDE-1–2), continuum dislocation dynamics (CDD)-based models (PDE-3–4), multi-field fluid and reaction–diffusion systems (PDE-5–6). Example simulations from all six models are shown in Fig. 5. Together they cover a range from simple scalar transport and diffusion to more complex systems such as Kolmogorov flow, Gray–Scott pattern formation, and the statistical evolution of systems of curved lines in continuum dislocation dynamics (CDD).

Table 1: Overview of the PDE models and resulting datasets. The column "Fields" refers to the number and type of continuous fields used for the numerical solution ("simulation"). The training dataset uses only *a single field* of that simulation as input to the ML model, cf. section 2.2.

No.	**Mathematical model**	**Simulation**		Training	
		Equation	**Fields**	**Datasets**	**Features**
1	Advection of a distribution of blobs	PDE-1	1 (scalar)	DS-1	1 (concentration)
2	Diffusion of a distribution of blobs	PDE-2	1 (scalar)	DS-2	1 (concentration)
3	Expansion and diffusion of a distribution of loops (reduced CDD)	PDE-3	3 (1 scalar, 1 vector)	DS-3a, DS-3b	1 (total dislocation density)
4	Statistical evolution of systems of curved lines (CDD)	PDE-4	4 (2 scalars, 1 vector)	DS-4	1 (total dislocation density)
5	Kolmogorov flow (Navier–Stokes, vorticity formulation)	PDE-5	2 (1 vector)	DS-5	1 (vorticity)
6	Reaction–diffusion (Gray–Scott model)	PDE-6	2 (scalar)	DS-6a, DS-6b, DS-6c, DS-6d	1 (concentration)

To keep comparisons uniform and to mimic partial observability in real measurements, we train all models on rollouts of a single representative scalar field per system (Table 1), even when the underlying PDE couples multiple state variables.

2.2 Neural network architecture

Our U-Net architecture is an extension of the original architecture by Ronneberger et al. (Ronneberger et al., 2015) and consists of two parts: an encoder (contracting path) that captures the spatial context of the input fields, and a decoder (expanding path) that enables precise localization of features. The input consists of a sequence of images, i.e., even though some of the original PDEs consist of multiple or vectorial field quantities, we only use a single, scalar field. The encoder comprises five stages, each with a double convolutional module followed by an average-pooling operator for downsampling. The decoder also contains five stages, each with a transposed convolution operator for upsampling followed by a double convolutional module. Between encoder and decoder we place a double convolutional module acting as a bottleneck.

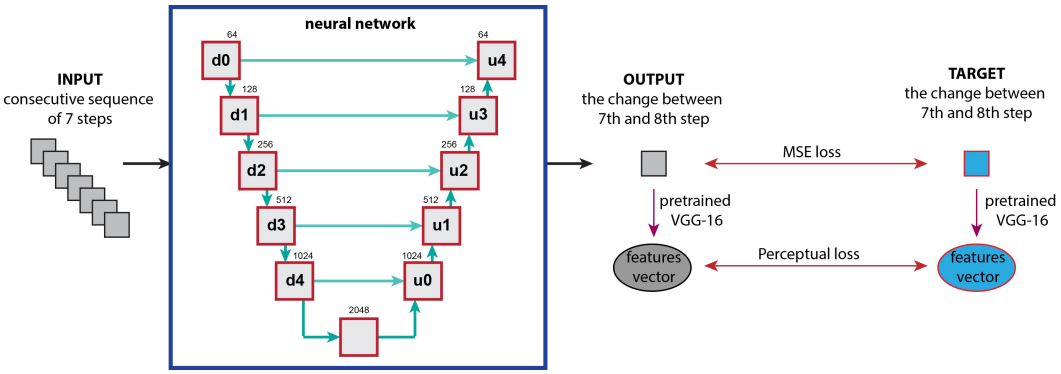

Figure 1: Illustration of the me-UNet architecture, showing the encoder–decoder structure, periodic padding, and multi-channel input/output setup for autoregressive time-stepping.

We denote by f_θ the parametric mapping implemented by a given architecture, with trainable parameters θ. All architectures considered in this paper, including me-UNet and the baselines, are trained in an *incremental* or residual form. Given an input sequence of L past fields

$$\{u^{n-L+1}, \ldots, u^n\} \subset \mathbb{R}^{H \times W}, \tag{1}$$

the network does not predict the next field u^{n+1} directly. Instead, it predicts a temporal update

$$\Delta u^{n+1} = f_\theta\big(u^{n-L+1}, \ldots, u^n\big), \tag{2}$$

and the next state is obtained as

$$u^{n+1} = u^n + \Delta u^{n+1}. \tag{3}$$

Thus, for $L = 7$ the output image represents the change in the field between the 7^{th} and 8^{th} time step. This residual-style parameterization empirically stabilizes long autoregressive rollouts and encourages the network to focus on learning short-time dynamics rather than absolute field values.

To enable a fair comparison with other architectures, we keep the input sequence length (seven consecutive time steps), the incremental output representation in equation 3, and the loss function fixed across models. Only the internal architecture of the mapping f_θ is changed. Specifically, in addition to me-UNet we adapt four alternative architectures: a vision transformer (ViT) (Dosovitskiy et al., 2020), an adaptive Fourier neural operator (AFNO), which is the core architecture of FourCastNet (Pathak et al., 2022), the PDE-Transformer (PDE-T) (Holzschuh et al., 2025), and a KAN-UNet in which the double convolutional layers of U-Net are replaced by KAN convolutional layers (Gao, 2024).

During training we minimize a combination of a pixel-wise loss $\mathcal{L}_{\text{MSE}}$ and a perceptual loss $\mathcal{L}_{\text{pc}}$. The total loss $\mathcal{L}$ for a predicted field $\hat{y}$ and reference field y is

$$\mathcal{L}(\hat{y}, y) = \mathcal{L}_{\text{MSE}}(\hat{y}, y) + \lambda_{\text{pc}}\, \mathcal{L}_{\text{pc}}(\hat{y}, y), \tag{4}$$

where $\mathcal{L}_{\text{MSE}}$ is the mean-squared error defined in eq. (5), and $\mathcal{L}_{\text{pc}}$ is the perceptual loss based on feature maps Φ_i of a pre-trained VGG-16 network as in eq. (6). In all experiments we keep the VGG-16 weights fixed and use feature maps from layer `relu2_2`, and we set $\lambda_{\text{pc}} = 1$.

3 Results

We now evaluate the performance of the different architectures on the PDE-generated datasets described in section 2.1 and appendix A.3. Our goal is not to obtain the lowest possible error on a single benchmark by combining a very large model with massive training data. Instead, we focus on a realistic small-data regime with autoregressive rollouts of $T = 100$ time steps. All models are trained with the common setup described in appendix A.4.1. For each dataset and architecture we train a separate model and generate autoregressive predictions starting from seven ground-truth snapshots; these seven frames form the input sequence, and the model predicts increments for the subsequent $T = 100$ time steps.

3.1 IN-DISTRIBUTION PREDICTION

We first consider in-distribution prediction, where training and test simulations are drawn from the same distribution of initial conditions for each PDE. For each dataset and architecture, we generate rollouts of length $T = 100$ and compute the root mean square error (RMSE) and spectral similarity defined in appendix A.4.2.

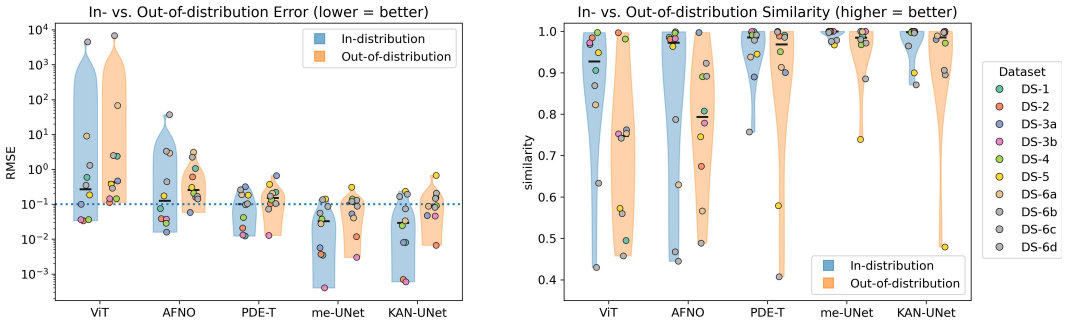

Figure 2: Comparison of average values over $T = 100$ time steps: Left panel visualize RMSE and right panel visualize cosine-similarity scores of the power spectral density (PSD).

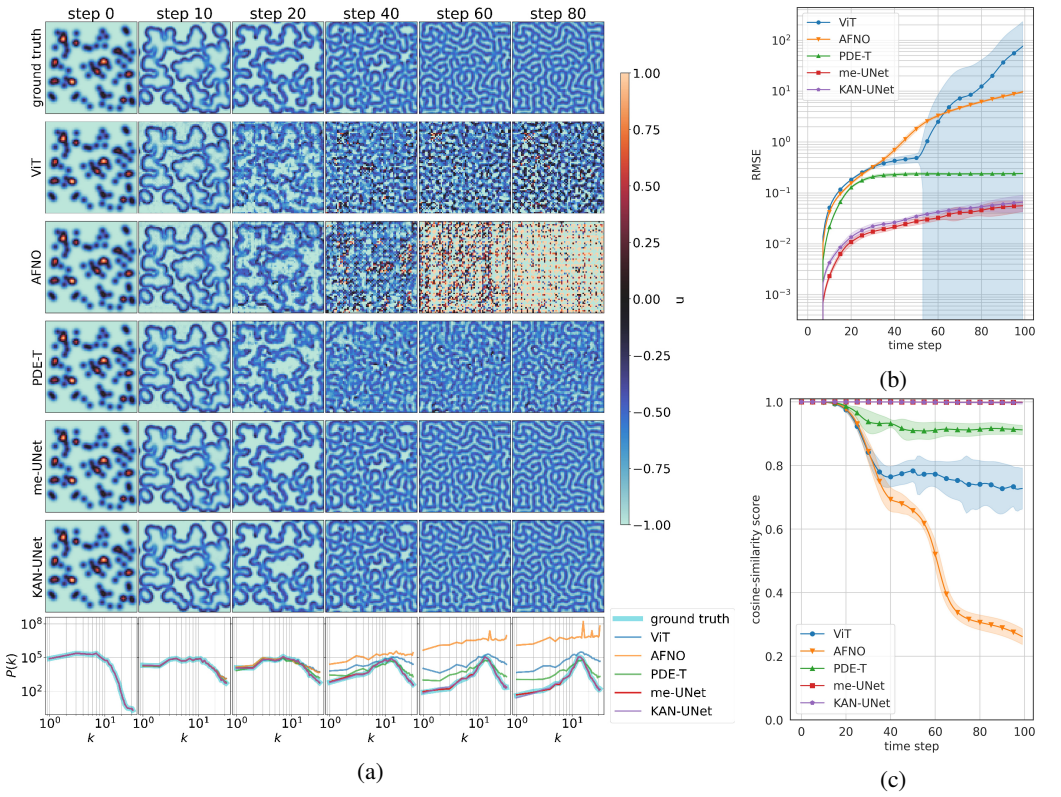

Figure 3: Performance of the different neural network architectures on the Gray–Scott dataset DS-6a: (a) example autoregressive rollouts; (b) per-time-step RMSE; and (c) cosine similarity of the PSD curves between prediction and reference.

Figure 2 presents an overview of in-distribution and OOD performance across all datasets: panel (a) shows the average RMSE over $T = 100$ prediction steps, and panel (b) shows the corresponding average PSD cosine similarity. Lower RMSE indicates better field-space accuracy, while cosine similarity values closer to 1 indicate a closer match of the spatial frequency content.

Overall, me-UNet achieves the lowest RMSE on almost all datasets. In particular, its average RMSE on DS-1, DS-3a, DS-3b, DS-5, DS-6a, DS-6b, DS-6c, and DS-6d is 0.0035, 0.0057, 0.0004, 0.1431, 0.0276, 0.0871, 0.1360, and 0.0554, respectively. The corresponding predicted snapshots show good agreement with the ground truth (see the me-UNet rows in Fig. 8a, Fig. 9a, Fig. 10a, Fig. 12a, Fig. 3a, Fig. 13a, Fig. 15a, and Fig. 14a). KAN-UNet achieves the lowest RMSE on DS-2 and DS-4 with 0.0007 and 0.0246, respectively (see the KAN-UNet rows in Fig. 8a and Fig. 11a).

In contrast, ViT attains the highest RMSE on several datasets (e.g., 0.5901 on DS-1, 9.1204 on DS-6a, and 4565.3740 on DS-6b), which is reflected in visibly degraded predictions (see the first rows of Fig. 7a, Fig. 3a, and Fig. 13a). PDE-Transformer performs worst on DS-3a (0.3182, see Fig. 9a), while AFNO shows the largest errors on DS-6c (0.4483) and DS-6d (3.3502).

Spectrally, me-UNet also consistently achieves the highest PSD cosine similarity, with values close to 1.0 across all datasets. KAN-UNet is typically the second-best model, with cosine similarity near 1.0 except on DS-5, where it attains 0.9. ViT and AFNO exhibit the lowest spectral similarity on the most challenging Gray–Scott datasets (e.g., 0.4298 and 0.4449 on DS-6b, and 0.4675 on DS-6d), indicating substantial distortion of the spatial frequency content over long rollouts.

In-distribution rollouts for all datasets are provided in Appendix A.6.1, together with the corresponding PSD curves and cosine similarity plots. Each figure contains snapshot sequences, per-time-step RMSE, and PSD cosine similarity for all architectures. In general, me-UNet produces stable pattern evolution with accurate spectral content, whereas several heavier architectures exhibit pattern drift and loss of small-scale structures.

3.2 OOD PREDICTION

We now investigate OOD prediction performance on the mentioned datasets. An overview of OOD performance across architectures is given in Fig. 2, which summarizes average RMSE and PSD cosine similarity for all datasets OOD tests. me-UNet exhibits the most consistent behavior, with relatively small degradation from in-distribution to OOD initial conditions, while several baselines show substantial increases in error or spectral mismatch on at least one of the two systems. Out-of-distribution rollouts are provided in Appendix A.6.2.

For CDD (DS-3a, DS-3b and DS-4), we train on simulations with a very large number of superimposed blob- and loop-like initial patterns, resulting in images where the individual blobs or loops can no longer be identified. Testing is then performed on configurations with a very small number of loops or with mixed line and loop arrangements, which are visually very different from the training data. Figures 20 illustrate such OOD cases. The main physical phenomenon—expansion of dislocation loops throughout the domain—is captured by most trained networks, and the predicted patterns remain close to the reference for me-UNet and KAN-UNet. The PSD curves in the last rows of Fig. 20 show a good match across a wide range of frequencies, with only small deviations at high frequencies for the best-performing models. AFNO, however, exhibits unstable behavior as time progresses (see the third rows of Fig. 20), leading to the highest RMSE values of 0.2353 and 0.2071 in the two OOD tests, as well as the lowest cosine similarities (0.9485 and 0.8907, see Fig. 2b). The fact that me-UNet can extrapolate from densely populated microstructures to sparse, geometrically simple initial conditions strongly suggests that it has learned the underlying dislocation dynamics rather than merely memorizing typical training configurations.

For DS-1, DS-2 and the Gray–Scott system (DS-6a–d), we train on randomly perturbed initial states and test on structured line initial conditions that differ strongly from the training distribution (e.g. compared first column of 3 and 4). Figures 4, 16, 17, 22, 24 and 23 show OOD rollouts for line initial patterns. Transformer-based models such as ViT, AFNO, and PDE-Transformer already struggle to train in-distribution on DS-6a or DS-6d and therefore perform poorly on OOD initial conditions; their predictions are very noisy and quickly diverge from the ground truth (see the second, third, and fourth columns of Fig. 4).

In contrast, me-UNet and KAN-UNet produce qualitatively correct OOD dynamics, capturing the reaction–diffusion behavior and generating patterns that remain similar to the reference (e.g. fifth and sixth columns of Fig. 4. For me-UNet, the RMSE is lowest among all models (0.0404 and 0.0425 for the two OOD cases), and the cosine similarity is highest (0.9992 and 0.9851, see Fig. 2b). Some noise appears at later time steps due to accumulated prediction errors, but the overall patterns

remain stable. ViT attains the highest RMSE (67.3472 and 205.6902), and AFNO reaches the lowest cosine similarities (0.5665 and 0.4419), indicating severe breakdown of OOD generalization for these heavy architectures.

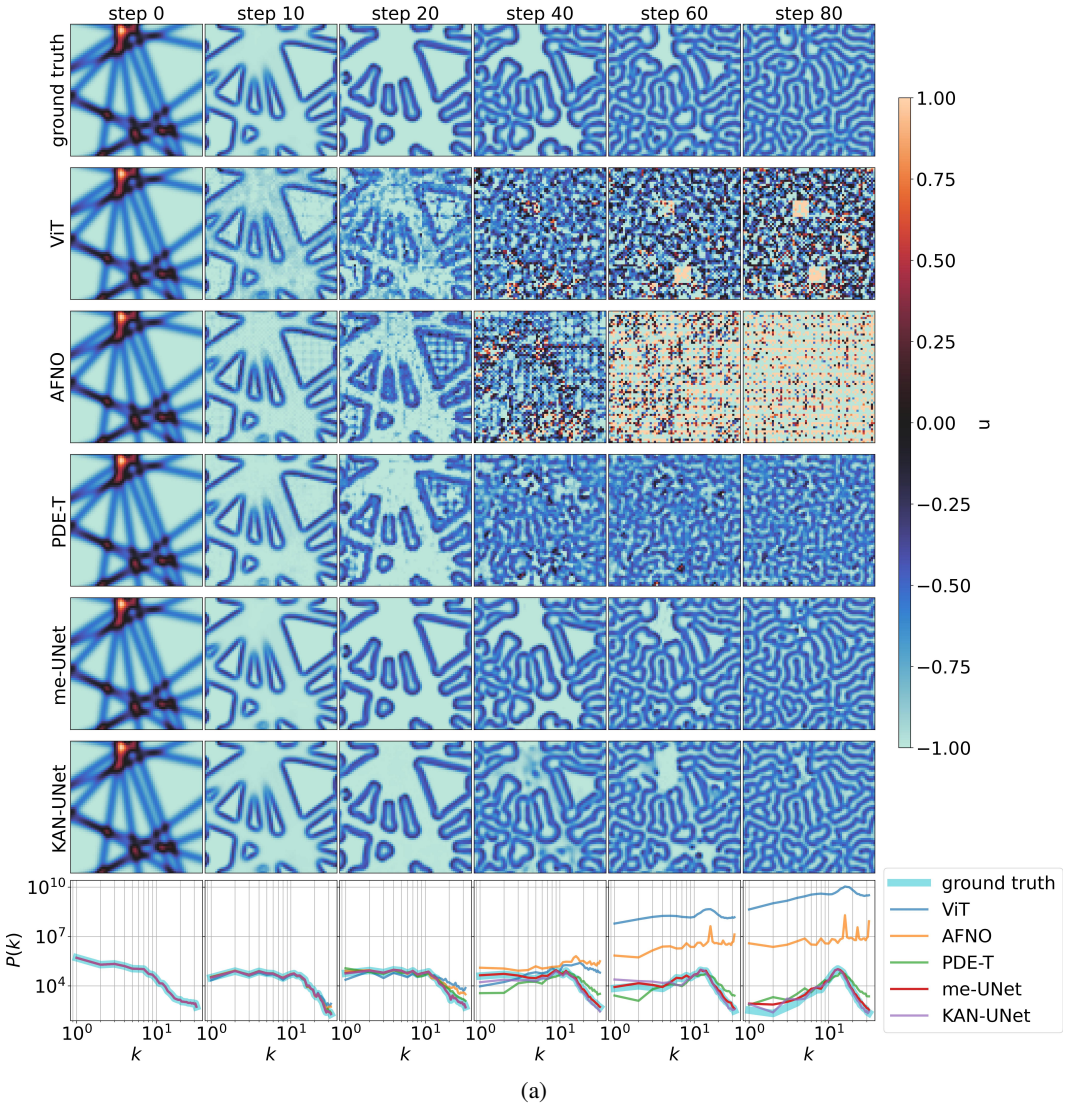

(a)

Figure 4: Performance of the different neural network architectures on the Gray–Scott dataset DS-6a.

4 Discussion

Our experiments provide a comparative picture of how different deep-learning architectures behave as surrogates for 2D periodic PDEs in a small-data regime. Across all five PDE families, the proposed me-UNet achieves consistently low field-space error and high spectral similarity for in-distribution rollouts and remains stable over hundreds of time steps.

In the same setting, neural-operator and transformer-based models (AFNO, PDE- Transformer, ViT, KAN-UNet) display more heterogeneous behavior: some of them perform competitively on selected PDEs, but they are typically less robust across all datasets and more prone to the accumulation of high-frequency artifacts in long rollouts. When evaluated with physics-based metrics, me-UNet also tends to preserve conserved quantities such as energy (see Fig. 25c) and mass (see Fig. 25a and

Fig. 25d) more accurately than the competing architectures, which suggests that local convolutions with periodic padding constitute a favorable inductive bias for these periodic PDEs.

More concretely, me-UNet performs well across all datasets (DS-1, DS-2, DS-3a/b, DS-4, DS-5, DS-6a–d), which span models ranging from simple diffusion to more complex systems such as Navier–Stokes (Kolmogorov flow) and continuum dislocation dynamics, using a single set of hyperparameters. In contrast, the performance of the neural- operator and transformer-based baselines varies strongly between datasets when trained with the same hyperparameters. For example, ViT and AFNO are competitive on the CDD (DS-4, Fig. 11) and Kolmogorov flow (DS-5, Fig. 12) datasets, but their performance degrades substantially on the Gray–Scott variants DS-6a (Fig. 3), DS-6b (Fig. 13), DS-6c (Fig. 15) and DS-6d (Fig. 14), where they tend to produce noisy or unstable patterns.

Beyond in-distribution performance, our results indicate that purely data- driven models can capture qualitative aspects of the dynamics even for initial conditions that differ substantially from those seen during training. For example, in the CDD OOD experiments shown in Fig. 20, the learned models reproduce the expansion and motion of individual loops or lines, although the training data (Fig. 11) contain only highly crowded superpositions in which the motion of individual objects is not visually apparent. The fact that me-UNet generalizes from these visually complex initial states to much simpler line- and loop-like configurations strongly suggests that it has internalized the underlying dislocation dynamics rather than merely memorizing typical microstructure textures.

Our notion of out-of-distribution generalization is deliberately restricted to initial-condition shifts within a fixed PDE and parameter regime on periodic domains, as defined in Section A.3. We do not claim generalization across PDE families, parameter ranges, domain geometries, boundary conditions, or resolutions; extending the benchmark and architectures to such forms of distribution shift (parameter OOD, PDE-family OOD, and domain OOD) is an important direction for future work.

Additionally, me-UNet works well with a relatively small amount of data. Based on the experimental results shown in Fig. 6b, sufficient performance on CDD is obtained with only 20 training simulations. While many works require a substantially larger number of simulations for training—for example, (Oommen et al., 2022) use 2000 simulations to train DEEPONET, and the smallest number of simulations in (Kontolati et al., 2024) is more than 260—our results suggest that, at least for CDD, a modest number of simulations can suffice when using an architecture with appropriate inductive biases. Furthermore, the time required for training me-UNet is much lower than that of the state-of-the-art architectures considered here. Training from scratch for 1000 epochs with a batch size of 40 on an NVIDIA RTX A6000 GPU takes roughly 5 hours for me-UNet, while ViT, AFNO, PDE-Transformer, and KAN-UNet take approximately 6, 42, 12, and 9 hours, respectively.

Notably, several of the benchmarks are only partially observed during training (one scalar field per system; cf. Table 1). The strong performance of me-UNet suggests that short temporal context can provide an effective data-driven closure for the chosen observable in these periodic small-data regimes.

This benchmark is deliberately scoped to highlight small-data autoregressive forecasting on 2D periodic grids, which leaves several important extensions open. First, all experiments are carried out on two-dimensional, structured, periodic grids with a fixed spatial resolution. While this setting is representative of many canonical benchmarks, it does not cover unstructured meshes, complex geometries, or adaptive resolution. Second, the architectures are trained separately for each PDE family rather than as a single multi-task model, and we have not attempted extensive per-architecture hyperparameter tuning beyond a common training protocol. Third, although we incorporate physics-based metrics that quantify the conservation of selected invariants and show that me-UNet can preserve them reasonably well, we only *encode periodic boundary conditions* explicitly, via periodic padding; we do not impose any hard conservation constraints in the architecture or loss. Future work could combine the periodic U-Net backbone with physics-informed loss terms or hard constraints to more strictly enforce mass, energy, or other invariants, and could explore similar inductive biases within neural-operator architectures designed for more general domains.

In addition, me-UNet, like most traditional CNN-based approaches, is naturally suited to image-like datasets where values are distributed on a structured grid, because it relies on fixed filter kernels (e.g., a 3×3 kernel for most 2D convolutional operators). Such architectures struggle to handle

unstructured grids with irregular shapes and non-uniform node distributions. To address this, it may be necessary either to combine me-UNet with techniques that transform an unstructured grid into a structured grid, such as space- filling curves (Heaney et al., 2024), or to use graph convolutional networks (Jiang et al., 2019) to perform convolution-like operations on irregular data. Furthermore, the current version of me-UNet is still limited to 2D simulation results; however, there is room to extend the architecture to 3D problems, which will be the next step following this work.

Finally, we emphasize again that in this work PDEs serve both as scientifically important models and as controlled, interpretable generators of high-dimensional spatio-temporal data. A surrogate model that cannot robustly learn dynamics generated by well-posed PDEs under controlled numerical conditions is unlikely to succeed on heterogeneous, noisy measurement data where the governing equations are only approximately known. Conversely, architectures that perform well under the small-data and OOD-initial- condition regime studied here are promising candidates for subsequent evaluation on real experimental and observational datasets.

Limitations: Our study focuses on out-of-distribution generalization under initial-condition shifts while keeping the underlying PDE, parameters, numerical solver, and spatial resolution fixed. We therefore do not evaluate robustness to other distribution shifts such as changes in PDE coefficients, forcing terms, boundary conditions, discretization, or measurement noise. In addition, our per-simulation normalization uses statistics computed over each simulated trajectory, which may not reflect strictly causal preprocessing in all deployment settings.

5 Conclusion

We have presented a systematic empirical study of autoregressive deep-learning surrogates for two-dimensional periodic PDEs in a small-data regime. Across the forementioned representative PDE families, we compared the proposed me-UNet to several recent neural-operator and transformer-based architectures under a common training protocol. Using field-space error, spectral similarity, and physics-based metrics to quantify the preservation of invariants such as energy and mass, we found that me-UNet consistently provides accurate and stable rollouts for in-distribution test cases while requiring substantially less training time than the competing architectures.

Within the considered setting, me-UNet also exhibits robust generalization to out-of-distribution initial conditions whose spatial structure differs markedly from the training data, including cases where the training set consists of highly crowded microstructures and the tests involve only a few well-separated objects. Together with the data-efficiency experiments, this supports the view that strong inductive biases in convolutional U-Nets—local filters, translation equivariance, multi-scale feature aggregation, and periodic padding that matches the boundary conditions—can be more beneficial than additional model complexity when data are scarce and the underlying dynamics are smooth on periodic domains.

At the same time, PDEs in this work serve as controlled, interpretable generators of high-dimensional spatio-temporal data, and we expect that the same architectural and evaluation principles will also be relevant for surrogate modeling and forecasting in other domains where the dynamics are described by, or well approximated by, continuum models and related dynamical systems.

Author Contributions

BDN proposed the initial me-UNet architecture, implemented all models, generated the datasets, and ran all experiments. BDN and SS jointly analyzed the data and wrote the manuscript. SS guided the design of the study.

Acknowledgments

The authors acknowledge funding by the Helmholtz Foundation Model Initiative supported by the Helmholtz Association.

REFERENCES

Felix Dietrich and Wil Schilders. Scientific machine learning. *Mathematische Semesterberichte*, 72 (2):89–115, 2025. doi: 10.1007/s00591-025-00399-4.

MWM Gamini Dissanayake and Nhan Phan-Thien. Neural-network-based approximations for solving partial differential equations. *communications in Numerical Methods in Engineering*, 10(3): 195–201, 1994. doi: https://doi.org/10.1002/cnm.1640100303.

Alexey Dosovitskiy, Lucas Beyer, Alexander Kolesnikov, Dirk Weissenborn, Xiaohua Zhai, Thomas Unterthiner, Mostafa Dehghani, Matthias Minderer, Georg Heigold, Sylvain Gelly, et al. An image is worth 16x16 words: Transformers for image recognition at scale. *arXiv preprint arXiv:2010.11929*, 2020. doi: https://doi.org/10.48550/arXiv.2010.11929.

Albert Einstein. Die Feldgleichungen der Gravitation. *Sitzungsberichte der Königlich Preußischen Akademie der Wissenschaften*, pp. 844–847, 1915. doi: https://adsabs.harvard.edu/pdf/1915SPAW.....844E.

Xiangbo Gao. Ka-conv: Kolmogorov-arnold convolutional networks with various basis functions. `https://github.com/XiangboGaoBarry/KA-Conv`, 2024.

Claire E Heaney, Yuling Li, Omar K Matar, and Christopher C Pain. Applying convolutional neural networks to data on unstructured meshes with space-filling curves. *Neural Networks*, 175:106198, 2024. doi: https://doi.org/10.1016/j.neunet.2024.106198.

Benjamin Holzschuh, Qiang Liu, Georg Kohl, and Nils Thuerey. Pde-transformer: Efficient and versatile transformers for physics simulations. 2025.

Kurt Hornik, Maxwell Stinchcombe, and Halbert White. Multilayer feedforward networks are universal approximators. *Neural Networks*, 2(5):359–366, 1989. ISSN 0893-6080. doi: 10.1016/0893-6080(89)90020-8.

Bo Jiang, Ziyan Zhang, Doudou Lin, Jin Tang, and Bin Luo. Semi-supervised learning with graph learning-convolutional networks. In *Proceedings of the IEEE/CVF conference on computer vision and pattern recognition*, pp. 11313–11320, 2019.

Justin Johnson, Alexandre Alahi, and Li Fei-Fei. Perceptual losses for real-time style transfer and super-resolution. In *Computer Vision–ECCV 2016: 14th European Conference, Amsterdam, The Netherlands, October 11-14, 2016, Proceedings, Part II 14*, pp. 694–711. Springer, 2016. doi: https://doi.org/10.1007/978-3-319-46475-6_43.

Dmitrii Kochkov, Jamie A Smith, Ayya Alieva, Qing Wang, Michael P Brenner, and Stephan Hoyer. Machine learning–accelerated computational fluid dynamics. *Proceedings of the National Academy of Sciences*, 118(21):e2101784118, 2021. doi: https://doi.org/10.1073/pnas.2101784118.

Felix Koehler, Simon Niedermayr, Ruediger Westermann, and Nils Thuerey. APEBench: A benchmark for autoregressive neural emulators of PDEs. *Advances in Neural Information Processing Systems (NeurIPS)*, 38, 2024.

Katiana Kontolati, Somdatta Goswami, George Em Karniadakis, and Michael D Shields. Learning nonlinear operators in latent spaces for real-time predictions of complex dynamics in physical systems. *Nature Communications*, 15(1):5101, 2024. doi: https://doi.org/10.1038/s41467-024-49411-w.

Isaac E. Lagaris, Aristidis Likas, and Dimitrios I. Fotiadis. Artificial neural networks for solving ordinary and partial differential equations. *IEEE Transactions on Neural Networks*, 9(5):987–1000, 1998. ISSN 1045-9227. doi: 10.1109/72.712178.

Hyuk Lee and In Seok Kang. Neural algorithm for solving differential equations. *Journal of Computational Physics*, 91(1):110–131, 1990. doi: https://doi.org/10.1016/0021-9991(90)90007-N.

Zongyi Li, Nikola Kovachki, Kamyar Azizzadenesheli, Burigede Liu, Kaushik Bhattacharya, Andrew Stuart, and Anima Anandkumar. Fourier neural operator for parametric partial differential equations. *arXiv preprint arXiv:2010.08895*, 2020. doi: https://arxiv.org/pdf/2010.08895.

Anders Logg, Kent-Andre Mardal, and Garth Wells. *Automated solution of differential equations by the finite element method: The FEniCS book*, volume 84. Springer Science & Business Media, 2012.

Lu Lu, Pengzhan Jin, Guofei Pang, Zhongqiang Zhang, and George Em Karniadakis. Learning nonlinear operators via deeponet based on the universal approximation theorem of operators. *Nature machine intelligence*, 3(3):218–229, 2021. doi: https://doi.org/10.1038/s42256-021-00302-5.

CLMH Navier. Sur les lois des mouvement des fluides, en ayant egard a l'adhesion des molecules. In *Annales de Chimie et de Physique*, volume 19, pp. 1821. Lavoisier Paris, France, 1821.

Binh Duong Nguyen, Pavlo Potapenko, Aytekin Demirci, Kishan Govind, Sébastien Bompas, and Stefan Sandfeld. Efficient surrogate models for materials science simulations: Machine learning-based prediction of microstructure properties. *Machine Learning with Applications*, pp. 100544, March 2024. ISSN 26668270. doi: 10.1016/j.mlwa.2024.100544. URL `https://linkinghub.elsevier.com/retrieve/pii/S2666827024000203`.

Vivek Oommen, Khemraj Shukla, Somdatta Goswami, Rémi Dingreville, and George Em Karniadakis. Learning two-phase microstructure evolution using neural operators and autoencoder architectures. *npj Computational Materials*, 8(1):190, 2022. doi: https://doi.org/10.1038/s41524-022-00876-7.

Adam Paszke, Sam Gross, Francisco Massa, Adam Lerer, James Bradbury, Gregory Chanan, Trevor Killeen, Zeming Lin, Natalia Gimelshein, Luca Antiga, et al. Pytorch: An imperative style, high-performance deep learning library. *Advances in neural information processing systems*, 32, 2019.

Jaideep Pathak, Shashank Subramanian, Peter Harrington, Sanjeev Raja, Ashesh Chattopadhyay, Morteza Mardani, Thorsten Kurth, David Hall, Zongyi Li, Kamyar Azizzadenesheli, et al. Fourcastnet: A global data-driven high-resolution weather model using adaptive fourier neural operators. *arXiv preprint arXiv:2202.11214*, 2022. doi: https://doi.org/10.48550/arXiv.2202.11214.

Maziar Raissi, Paris Perdikaris, and George E Karniadakis. Physics-informed neural networks: A deep learning framework for solving forward and inverse problems involving nonlinear partial differential equations. *Journal of Computational physics*, 378:686–707, 2019. doi: https://doi.org/10.1016/j.jcp.2018.10.045.

David A Randall, Cecilia M Bitz, Gokhan Danabasoglu, A Scott Denning, Peter R Gent, Andrew Gettelman, Stephen M Griffies, Peter Lynch, Hugh Morrison, Robert Pincus, et al. 100 years of earth system model development. *Meteorological Monographs*, 59:12–1, 2019.

Pu Ren, Chengping Rao, Yang Liu, Jian-Xun Wang, and Hao Sun. Phycrnet: Physics-informed convolutional-recurrent network for solving spatiotemporal pdes. *Computer Methods in Applied Mechanics and Engineering*, 389:114399, 2022. doi: https://doi.org/10.1016/j.cma.2021.114399.

Pu Ren, Chengping Rao, Yang Liu, Zihan Ma, Qi Wang, Jian-Xun Wang, and Hao Sun. Physr: Physics-informed deep super-resolution for spatiotemporal data. *Journal of Computational Physics*, 492:112438, 2023. doi: https://doi.org/10.1016/j.jcp.2023.112438.

Olaf Ronneberger, Philipp Fischer, and Thomas Brox. U-net: Convolutional networks for biomedical image segmentation. In *Medical image computing and computer-assisted intervention–MICCAI 2015: 18th international conference, Munich, Germany, October 5-9, 2015, proceedings, part III 18*, pp. 234–241. Springer, 2015. doi: https://doi.org/10.1007/978-3-319-24574-4_28.

Erwin Schrödinger. An undulatory theory of the mechanics of atoms and molecules. *Physical review*, 28(6):1049, 1926. doi: https://doi.org/10.1103/PhysRev.28.1049.

Khemraj Shukla, Patricio Clark Di Leoni, James Blackshire, Daniel Sparkman, and George Em Karniadakis. Physics-informed neural network for ultrasound nondestructive quantification of surface breaking cracks. *Journal of Nondestructive Evaluation*, 39(3):61, 2020. doi: https://doi.org/10.1007/s10921-020-00705-1.

Jingmin Sun, Yuxuan Liu, Zecheng Zhang, and Hayden Schaeffer. Towards a foundation model for partial differential equations: Multioperator learning and extrapolation. *Physical Review E*, 111 (3):035304, 2025. doi: https://doi.org/10.1103/PhysRevE.111.035304.

Mark Vogelsberger, Shy Genel, Volker Springel, Paul Torrey, Debora Sijacki, Dandan Xu, Greg Snyder, Dylan Nelson, and Lars Hernquist. Introducing the illustris project: simulating the coevolution of dark and visible matter in the universe. *Monthly Notices of the Royal Astronomical Society*, 444(2):1518–1547, 2014. doi: https://doi.org/10.1093/mnras/stu1536.

Jared Willard, Xiaowei Jia, Shaoming Xu, Michael Steinbach, and Vipin Kumar. Integrating scientific knowledge with machine learning for engineering and environmental systems. *ACM Computing Surveys*, 55(4):1–37, 2023. doi: 10.1145/3514228.

Biao Yuan, He Wang, Ana Heitor, and Xiaohui Chen. f-picnn: a physics-informed convolutional neural network for partial differential equations with space-time domain. *Journal of Computational Physics*, 515:113284, 2024. doi: https://doi.org/10.1016/j.jcp.2024.113284.

Dongkun Zhang, Ling Guo, and George Em Karniadakis. Learning in modal space: Solving time-dependent stochastic pdes using physics-informed neural networks. *SIAM Journal on Scientific Computing*, 42(2):A639–A665, 2020.

Yinhao Zhu, Nicholas Zabaras, Phaedon-Stelios Koutsourelakis, and Paris Perdikaris. Physics-constrained deep learning for high-dimensional surrogate modeling and uncertainty quantification without labeled data. *Journal of Computational Physics*, 394:56–81, 2019. doi: https://doi.org/10.1016/j.jcp.2019.05.024.

A Appendix

A.1 Description of the mathematical models

- **PDE-1–2: single-field linear transport and diffusion.** These are classical scalar advection and diffusion equations on periodic domains, used as basic test cases for forecasting and spectral fidelity.
- **PDE-3–4: continuum dislocation dynamics (CDD)-based models.** These models describe the transport and evolution of possibly curved line-segments via various continuum densities. PDE-3a and PDE-3b are reduced CDD systems that capture expansion and motion of dislocation loops in a simplified setting (with a smaller number of active fields and, in PDE-3a and 3b, curvature initialized to zero), whereas PDE-4 is the full three-field CDD model considered in Appendix 2.1 with an additional curvature density.
- **PDE-5–6: multi-field fluid and reaction–diffusion systems.** PDE-5 is a Navier–Stokes system in Kolmogorov-flow configuration, evaluated in terms of the scalar vorticity field, and PDE-6 is the Gray–Scott reaction–diffusion system with two reacting species.

A.2 Loss function

A.2.1 MSE loss

The mean-squared error (MSE) loss is widely used in the machine-learning community. It computes the average squared difference between the predicted and true values:

$$\mathcal{L}_{\mathrm{MSE}} = \frac{1}{N}\sum_{i=1}^{N}\big(\hat{y}_i - y_i\big)^2, \tag{5}$$

where N is the number of data points, y_i is the true value, and $\hat{y}_i$ is the predicted value for the i-th sample.

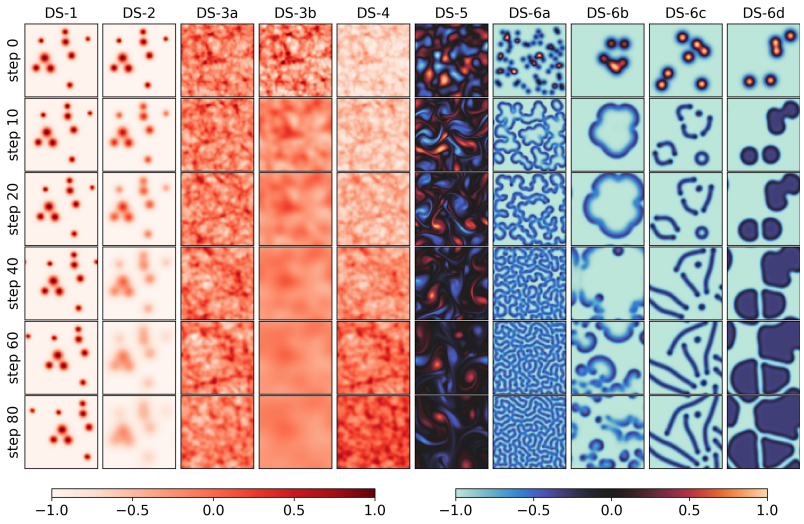

Figure 5: Examples of simulation results from all mathematical models. Datasets DS-1 and 2 are obtained from simple convection and diffusion equations, while the complexity of the PDEs and the number of involved state variables increases towards the right: DS-3a, 3b, and 4 are obtained from CDD PDEs, DS-5 from Navier-Stokes equations, while the variants of DS-6 are obtained from the Gray-Scott model.

A.2.2 Perceptual loss

Perceptual loss was introduced by Johnson et al. Johnson et al. (2016); it is computed based on features extracted from a pre-trained network rather than directly from pixel-wise differences. Perceptual loss captures more abstract and global image qualities that are often more relevant for human perception, whereas pixel-based losses such as MSE penalize local differences and can lead to overly smooth or blurry images:

$$\mathcal{L}_{\text{pc}} = \sum_i \left\| \Phi_i(\hat{y}) - \Phi_i(y) \right\|^2, \tag{6}$$

where Φ_i denotes the feature map from the i-th layer of the pre-trained network, and y and $\hat{y}$ are the true and predicted images, respectively. In this work, we use VGG-16 as the pre-trained network to obtain feature maps.

A.3 Simulation datasets and training samples

The dataset abbreviations are listed in Tab. 1: for PDE-1, 2, 4, 5 we obtain datasets DS-1, 2, 4 and 5; for PDE-3 we consider 2 parameter settings, denoted DS-3a and DS-3b; for PDE-6 we consider four different parameter settings, denoted DS-6a, DS-6b, DS-6c, and DS-6d. Each of the resulting 10 datasets consists of 110 simulations. Examples from each dataset are shown in Fig. 5, and detailed descriptions are given in the Appendix. For each dataset, 100 simulations are used for training/validating during training process with the split ratio 80/20, and the remaining 10 are kept untouched for testing. Each simulation contains 100 time steps.

For autoregressive training, the input data are constructed by sampling a random time index n with $7 \leq n \leq 99$ (using one-based indexing for time steps). For each such n, we stack the 7 consecutive fields

$$u^{n-6}, u^{n-5}, \ldots, u^n \tag{7}$$

along the channel dimension to form a multi-channel input image. The corresponding target is an *increment field* that represents the change between time steps n and $n+1$,

$$\Delta u^{n+1} = u^{n+1} - u^n. \tag{8}$$

Thus, our models are trained to predict Δu^{n+1} given the past sequence $\{u^{n-6}, \ldots, u^n\}$, rather than the absolute field u^{n+1}. During rollout, the next state is obtained via the residual update

$$\hat{u}^{n+1} = \hat{u}^n + \Delta\hat{u}^{n+1}, \tag{9}$$

where hats denote model predictions. Focusing on local temporal increments stabilizes long autoregressive rollouts: the network only needs to learn short-term corrections instead of reconstructing the full state, and it can concentrate on the dynamics of the system rather than on absolute field values. This residual parameterization empirically leads to substantially more stable long-horizon predictions, which is consistent with the fact that many PDE solutions change gradually between adjacent time steps.

All data values are scaled to the interval $[-1, 1]$ separately for each simulation and state variable. For a given state variable, the minimum and maximum over all time steps within a simulation are used to linearly map the values in each frame to the required range; scaling is not recomputed per frame. This per-simulation, per-variable normalization follows common practice in PDE surrogate modeling, but it can have drawbacks in multi-field systems, which we discuss later in Appendix B. All images are resized to 64×64 pixels.

In-distribution vs out-of-distribution initial conditions For each PDE family we fix the governing equations, physical parameters, numerical scheme, and spatial resolution. Training and test simulations always share this fixed configuration. The only source of distribution shift we study in this work is the distribution of initial conditions: "in-distribution" (ID) test rollouts use the same random initial-condition generator as training, whereas "out-of-distribution" (OOD) test rollouts use qualitatively different initial-condition families within the same PDE and parameter regime (e.g., sparse loops or line-like structures for CDD, or structured line/blob perturbations for Gray–Scott). Thus, throughout this paper, OOD refers specifically to shifts in the initial-condition distribution under a fixed PDE and parameter setting.

A.4 More details about training setup and evaluation metrics

A.4.1 Training setup

For each PDE dataset and each architecture, we train a separate model using the same training protocol. Unless otherwise stated, we use the Adam optimizer with an initial learning rate of 1×10^{-4}, weight decay 1×10^{-5}, and a batch size of 40. We train each models for 1000 epochs and report the checkpoint with lowest validation loss.

For me-UNet, the channel widths at the five encoder levels are $[64, 128, 256, 512, 1024]$ and mirrored in the decoder. For the baselines, we follow standard configurations adapted to our 64×64 input size: for ViT we use a patch size of 8, embedding dimension 768, depth 12, and 8 attention heads; for AFNO we use a patch size of 4, embedding dimension 768, depth 12, MLP ratio 4, and 16 AFNO blocks; for PDE-Transformer we use the PDE-B configuration of (Holzschuh et al., 2025); and for KAN- UNet we mirror the me-UNet channel widths in encoder and decoder, replacing the `Conv2d` layers in the double-convolution blocks by `FastKANConvLayer` modules with Chebyshev basis functions. All other architectural details are kept as close as possible to the original implementations referenced above.

Periodic boundary conditions are implemented in most of the mentioned architectures: in AFNO, periodic padding is used through an additional 2D convolutional layer (Pathak et al., 2022); PDE-Transformer mimics periodic boundary conditions by rolling the tokens along the x- and y-axis when shifting the attention windows (Holzschuh et al., 2025); KAN-UNet implements periodic padding similar to me-UNet. Only our implementation of the vision transformer use the vanilla architecture.

A.4.2 Evaluation metrics and physics-aware measures

We evaluate all models using three complementary criteria: (i) field-space error, (ii) spectral similarity, and (iii) physics-aware metrics that monitor conserved or prescribed global quantities.

Field-space error For each rollout we compute the RMSE between the predicted fields $\hat{y}$ and reference fields y, averaged over spatial grid points, output channels, and time steps:

$$\mathrm{RMSE} = \sqrt{\frac{1}{NTC} \sum_{t=1}^{T} \sum_{c=1}^{C} \sum_{i=1}^{N} \left(\hat{y}_{t,c,i} - y_{t,c,i}\right)^2}, \tag{10}$$

where N is the number of spatial grid points, C the number of state variables, and T the number of time steps in the rollout.

Spectral similarity To compare spatial frequency content we compute the azimuthally averaged power spectral density (PSD) for each snapshot and channel similar to what is done in (Koehler et al., 2024; Nguyen et al., 2024). Let $P_{t,c}(k)$ and $\hat{P}_{t,c}(k)$ denote the PSD of the reference and predicted fields, respectively, as a function of the radial wavenumber k (obtained by averaging $|\mathcal{F}[y_{t,c}]|^2$ and $|\mathcal{F}[\hat{y}_{t,c}]|^2$ over angular directions in Fourier space). For each time step t and channel c we then compute the cosine similarity

$$\mathrm{cos\_sim}_{t,c} = \frac{\sum_k \hat{P}_{t,c}(k)\, P_{t,c}(k)}{\sqrt{\sum_k \hat{P}_{t,c}(k)^2}\, \sqrt{\sum_k P_{t,c}(k)^2}}. \tag{11}$$

The reported spectral similarity is the mean of $\mathrm{cos\_sim}_{t,c}$ over channels and time steps.

Physics-based metrics In addition to these generic metrics we track physically meaningful global quantities for each PDE. All such quantities are defined as spatial integrals (or sums over grid points) of appropriate functions of the state variables. For Kolmogorov flow we monitor the kinetic energy $E(t)$ of the velocity field (obtained from the vorticity field) and compare the temporal evolution of $E(t)$ between reference and prediction. For the CDD model we monitor the spatial integral of the total dislocation density $\rho_t(t)$, which is known to follow a prescribed linear evolution according to the governing equations, and we assess how closely the learned surrogate reproduces this relationship. For Gray–Scott systems we track the total mass of the reactants (spatial integrals of u and v), which should remain approximately conserved up to reaction terms, and compare their evolution under the learned models. For the advection equations we track conservation of total mass, which should remain constant during transport up to numerical errors.

For each architecture and dataset we report summary statistics of these diagnostics over the rollout horizon in section 3. The normalized absolute errors of the monitored quantities are visualized in Fig. 25.

A.4.3 Software and implementation details

All neural-network models are implemented in PyTorch (Paszke et al., 2019) using Python 3.10.12. Experiments are run on a workstation equipped with an NVIDIA RTX A6000 GPU with 48 GB of memory and a multi-core CPU, using CUDA 12.8 and cuDNN 91002. The me-UNet architecture and training loops are implemented from scratch, while the baseline models (ViT, AFNO, PDE-Transformer, KAN-UNet) build on publicly available reference implementations that we adapt to our input–output format and loss functions.

The synthetic datasets are generated with finite-element and finite-volume solvers implemented in C++/Python using FEniCS (Logg et al., 2012) for PDE-1–PDE-4, JAX-CFD (Kochkov et al., 2021) for PDE-5, and exponax (Koehler et al., 2024) for PDE-6. For each PDE dataset we fix the numerical scheme, time step, and resolution as described in section 2.1 and appendix A.3. Random initial conditions are sampled using NumPy 1.26.4 with a fixed random seed, and we use consistent seeds across models to ensure that training and evaluation splits are identical.

All configuration files specifying all hyperparameters (learning rates, batch sizes, channel widths, etc.) are provided in the accompanying code repository. Where possible we also release pre-trained model checkpoints and scripts to regenerate all figures and tables from this paper, in order to facilitate reproducibility and further comparison.

A.5 DATA EFFICIENCY

Here we study data efficiency on the CDD dataset, which serves as a representative benchmark for evaluating how the architectures behave under data limitations. We do not repeat these ablations on all other datasets, but we expect qualitatively similar trends to hold.

We vary three factors: (i) the number of time steps per simulation used during training, (ii) the number of training simulations, and (iii) the input sequence length L (number of past time steps provided as context). For each setting we retrain all architectures with the same protocol as in appendix A.4.1 and evaluate in-distribution rollouts.

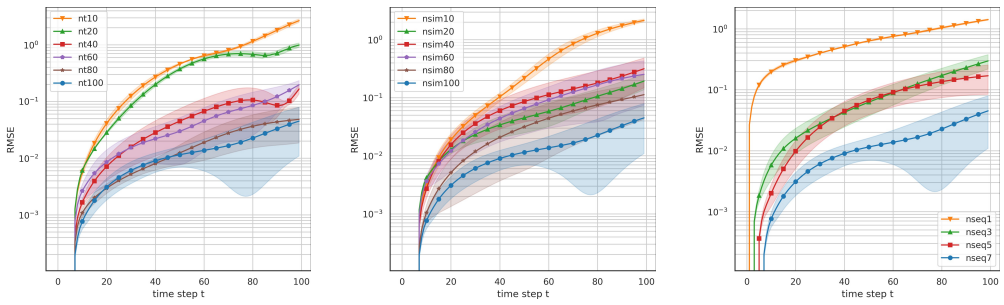

(a) (b) (c)

Figure 6: Data-efficiency study on the CDD dataset (DS-4): RMSE over 100-step rollouts as a function of (a) the number of time steps per simulation used during training, (b) the number of training simulations, and (c) the input sequence length L (number of past frames used as context).

Figure 6 summarizes the RMSE obtained under these variations. In panel (a), labels $\mathrm{nt}10$, $\mathrm{nt}20$, $\mathrm{nt}40$, $\mathrm{nt}60$, $\mathrm{nt}80$, and $\mathrm{nt}100$ indicate the number of time steps per simulation used to construct training samples (with the number of simulations fixed at 100 and the input sequence length at $L = 7$). We observe that training with 40 time steps per simulation is already sufficient for me-UNet and the better-performing baselines; using more time steps yields only marginal improvements in RMSE.

In panel (b), labels $\mathrm{nsim}10$, $\mathrm{nsim}20$, $\mathrm{nsim}40$, $\mathrm{nsim}60$, $\mathrm{nsim}80$, and $\mathrm{nsim}100$ indicate the number of simulations used for training (again with $L = 7$ and $T = 100$ time steps available). Here, me-UNet reaches a low-error regime with as few as 20 training simulations, with RMSE already close to the values obtained with 40, 60, or 80 simulations. In contrast, the transformer- and operator-based models benefit more noticeably from additional simulations, indicating that their data requirements are higher in this setting.

Finally, panel (c) varies the input sequence length $L \in \{1, 3, 5, 7\}$ while keeping the number of simulations and time steps fixed at 100. We find that using $L = 5$ or $L = 7$ input frames yields substantially lower RMSE than using a single-frame context ($L = 1$), confirming that limited temporal history is important for accurate next-step prediction. Performance saturates between $L = 5$ and $L = 7$, consistent with the choice of time step in the simulations: the dynamics change appreciably over a window of about six intervals, and longer contexts bring limited additional benefit.

Overall, these data-efficiency experiments show that, in the small-data regime, the convolutional inductive biases of me-UNet allow it to make more effective use of limited training data than the heavier baselines. They also provide practical guidance for selecting the number of simulations, time steps, and input sequence length in future studies on similar systems.

A.6 VISUALIZATION OF PREDICTION PERFORMANCE ACROSS ARCHITECTURES

This section contains additional qualitative rollouts and metric curves for all datasets, complementing the examples in section 3. Each figure shows, for a fixed dataset, autoregressive predictions of all architectures over 100 time steps together with per-time-step RMSE and PSD cosine similarity. These plots illustrate in more detail the trends discussed in the main text: me-UNet and, to a

lesser extent, KAN-UNet produce stable pattern evolution with low error and high spectral similarity, whereas several of the heavier architectures either smooth out fine-scale structure or develop high-frequency artifacts over long rollouts.

A.6.1 IN-DISTRIBUTION AUTOREGRESSIVE ROLLOUTS

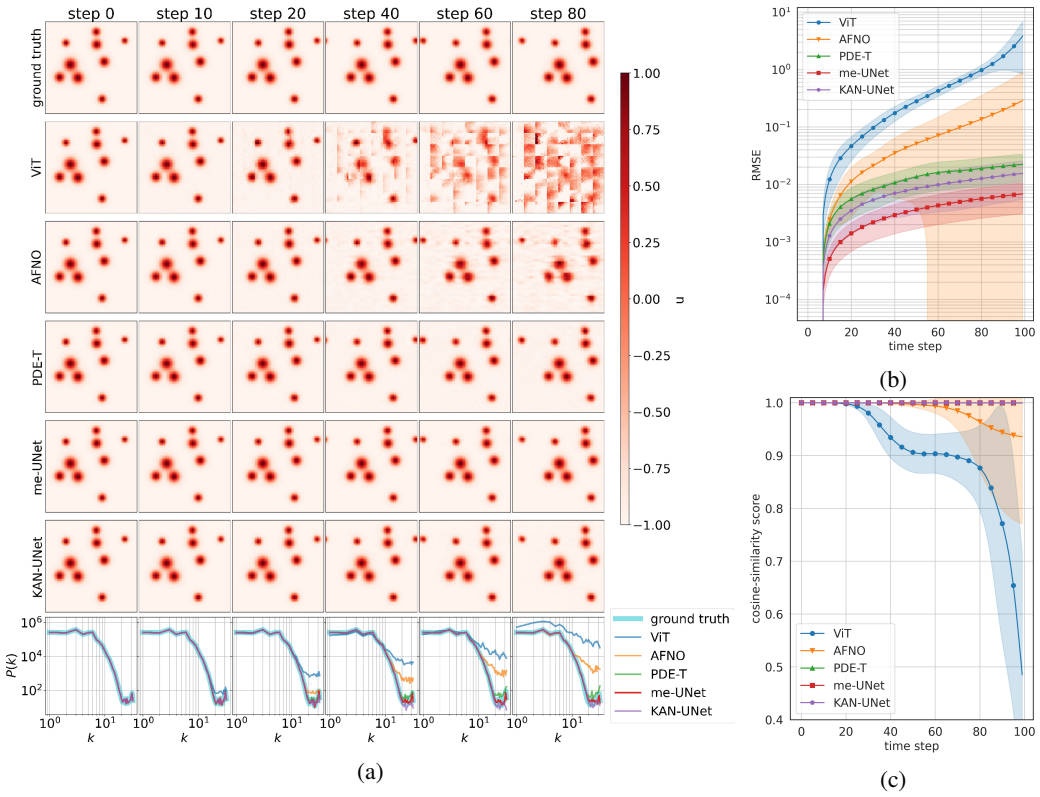

Figure 7: Visualization of the performance of the different neural networks on the DS-1 dataset: (a) autoregressive prediction results; (b) RMSE; and (c) cosine similarity of the PSD curves.

A.6.2 OOD AUTOREGRESSIVE ROLLOUTS

B VISUALIZATION OF PHYSICS-BASED METRICS ACROSS ARCHITECTURES

In this section we provide additional plots of the physics-based metrics introduced in appendix A.4.2 for in-distribution rollouts. Each panel in Fig. 25 shows the normalized absolute error of a conserved or approximately conserved quantity (e.g., mass, energy, total dislocation density) as a function of time for all architectures. Across the four datasets, me-UNet generally yields the smallest deviation from the reference curves over 100 time steps, with KAN-UNet often second-best, and the transformer- and operator-based models showing larger drift.

The accumulated error for DS-4 (Fig. 25b, Fig. 26a and Fig. 26b) may arise from the large range of values between the minimum and maximum of the original dataset (before scaling to $[-1, 1]$). Since the number of loops used as initial values spans a wide range (50–500 loops), the number of simulations may be relatively small compared to the variability in total line length. This can result in a systematic shift of the spatial integral of the state variable (see Fig. 26a,b). However, the main physical behavior of localization (i.e., the overall patterns) is still captured by the trained models (see Fig. 20).

For the other datasets, such as DS-6a (Fig. 25d, Fig. 26c and Fig. 26d), the minimum and maximum values of the original data for all simulations, both in-distribution and OOD, lie in a much narrower

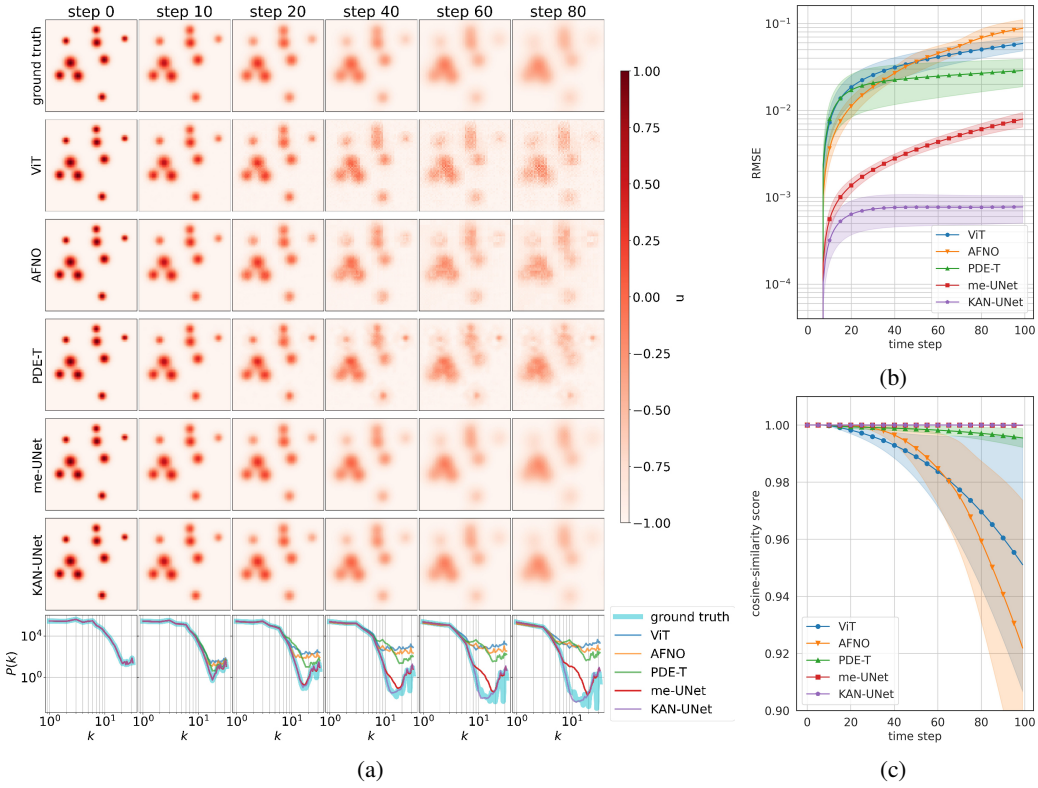

Figure 8: Visualization of the performance of the different neural networks on the DS-2 dataset: (a) autoregressive prediction results; (b) RMSE; and (c) cosine similarity of the PSD curves.

range. In these cases, the physical phenomena are well captured, both in terms of localization and generalization behavior (see Fig. 4, Fig. 26c,d).

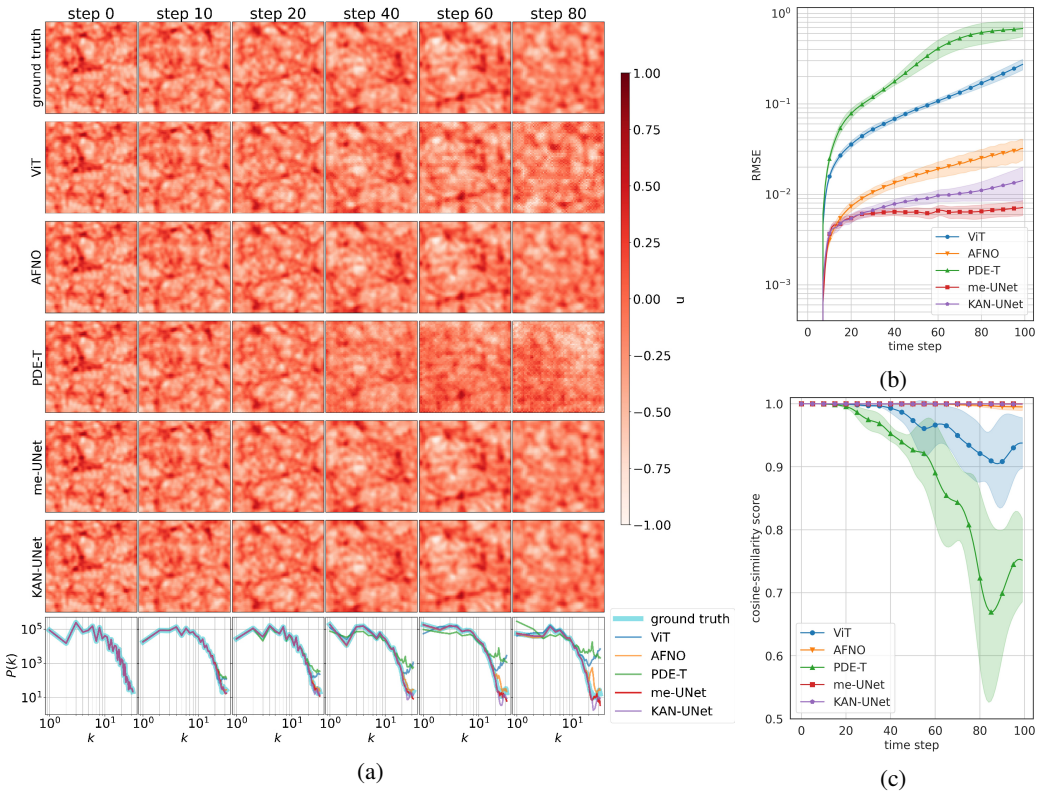

Figure 9: Visualization of the performance of the different neural networks on the DS-3a dataset: (a) autoregressive prediction results; (b) RMSE; and (c) cosine similarity of the PSD curves.

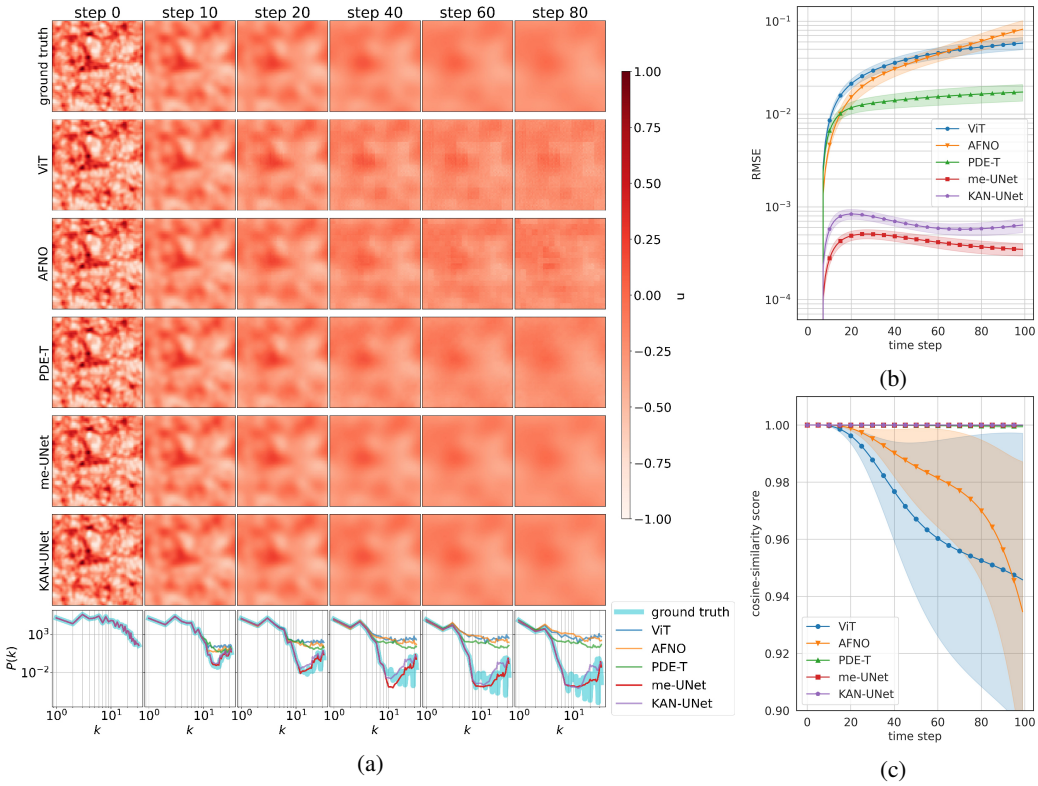

Figure 10: Visualization of the performance of the different neural networks on the DS-3b dataset: (a) autoregressive prediction results; (b) RMSE; and (c) cosine similarity of the PSD curves.

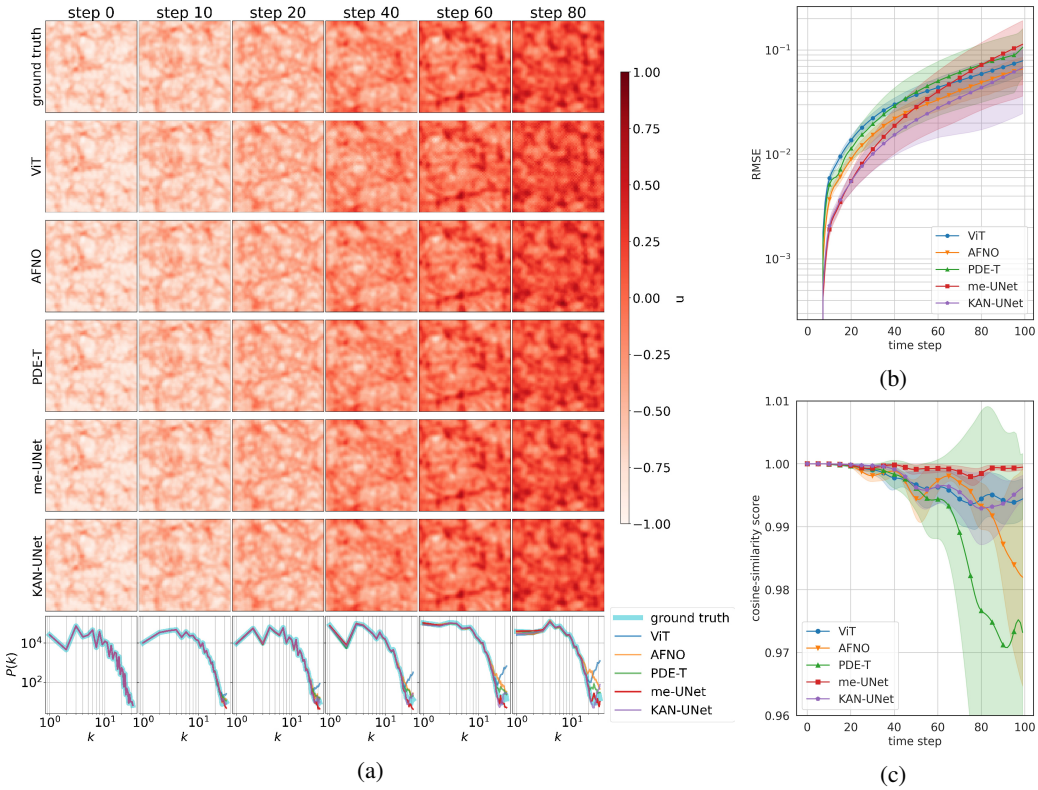

Figure 11: Performance of the different neural network architectures on the CDD dataset (DS-4): (a) example autoregressive rollouts; (b) per-time-step RMSE; and (c) cosine similarity of the PSD curves between prediction and reference.

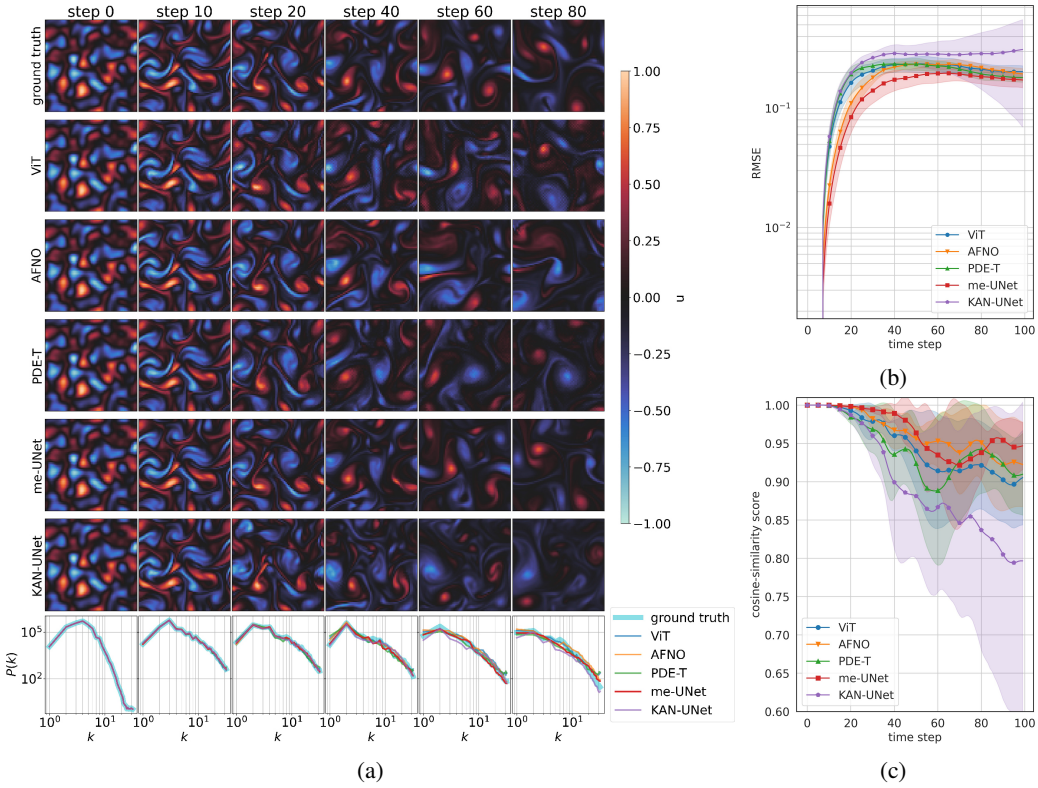

Figure 12: Visualization of the performance of the different neural networks on the DS-5 dataset: (a) autoregressive prediction results; (b) RMSE; and (c) cosine similarity of the PSD curves.

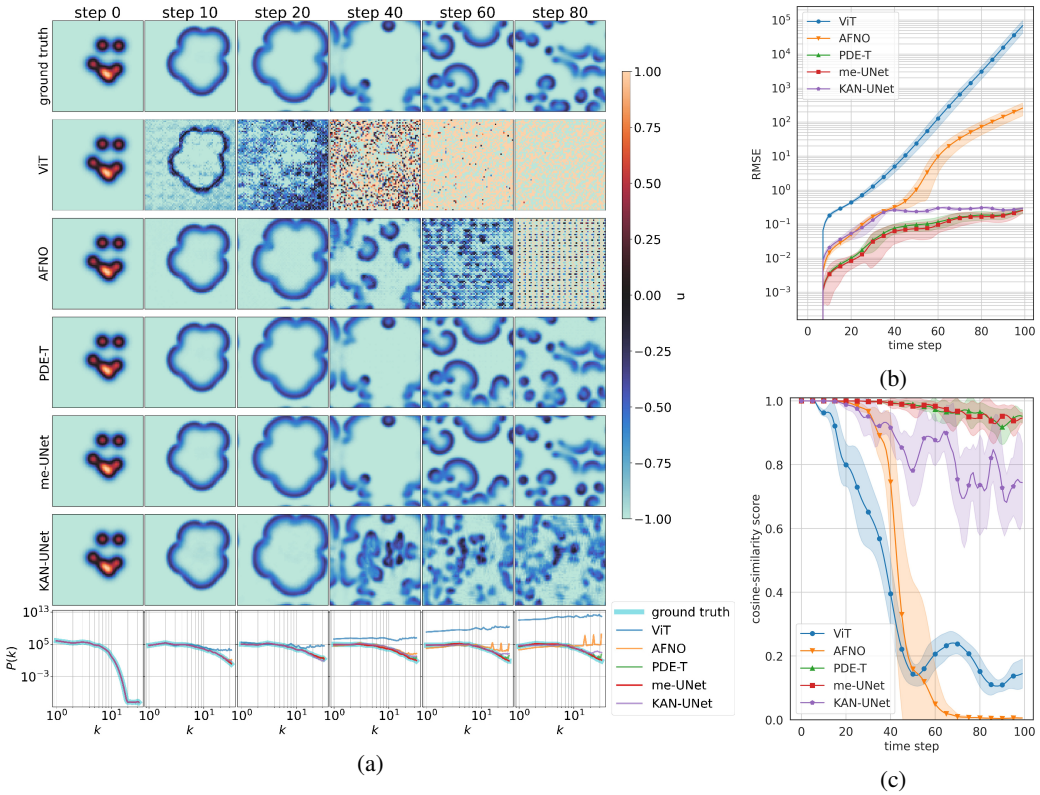

Figure 13: Visualization of the performance of the different neural networks on the DS-6b dataset: (a) autoregressive prediction results; (b) RMSE; and (c) cosine similarity of the PSD curves.

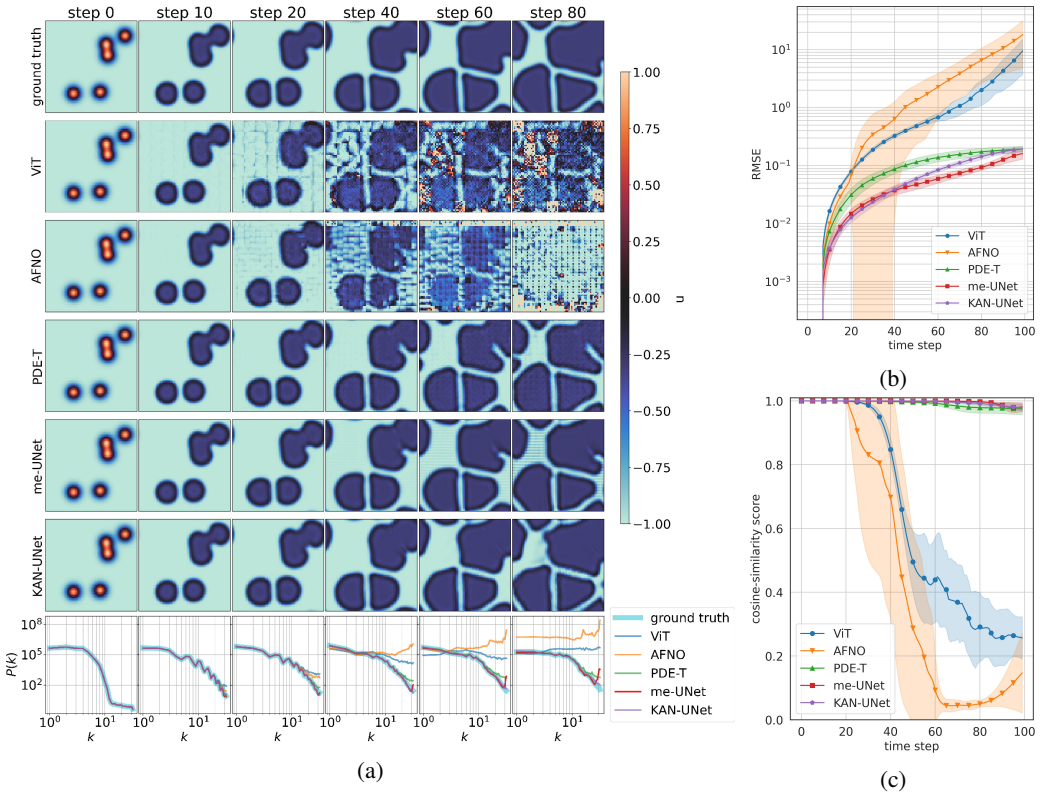

Figure 14: Visualization of the performance of the different neural networks on the DS-6c dataset: (a) autoregressive prediction results; (b) RMSE; and (c) cosine similarity of the PSD curves.

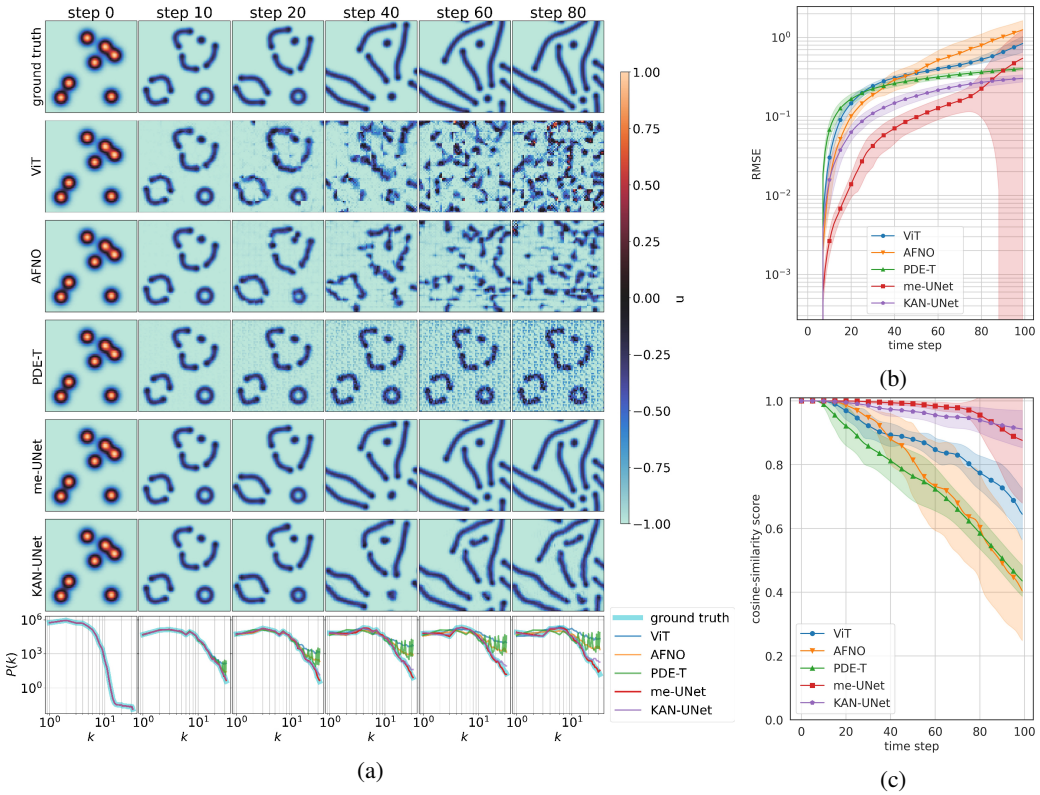

Figure 15: Visualization of the performance of the different neural networks on the DS-6d dataset: (a) autoregressive prediction results; (b) RMSE; and (c) cosine similarity of the PSD curves.

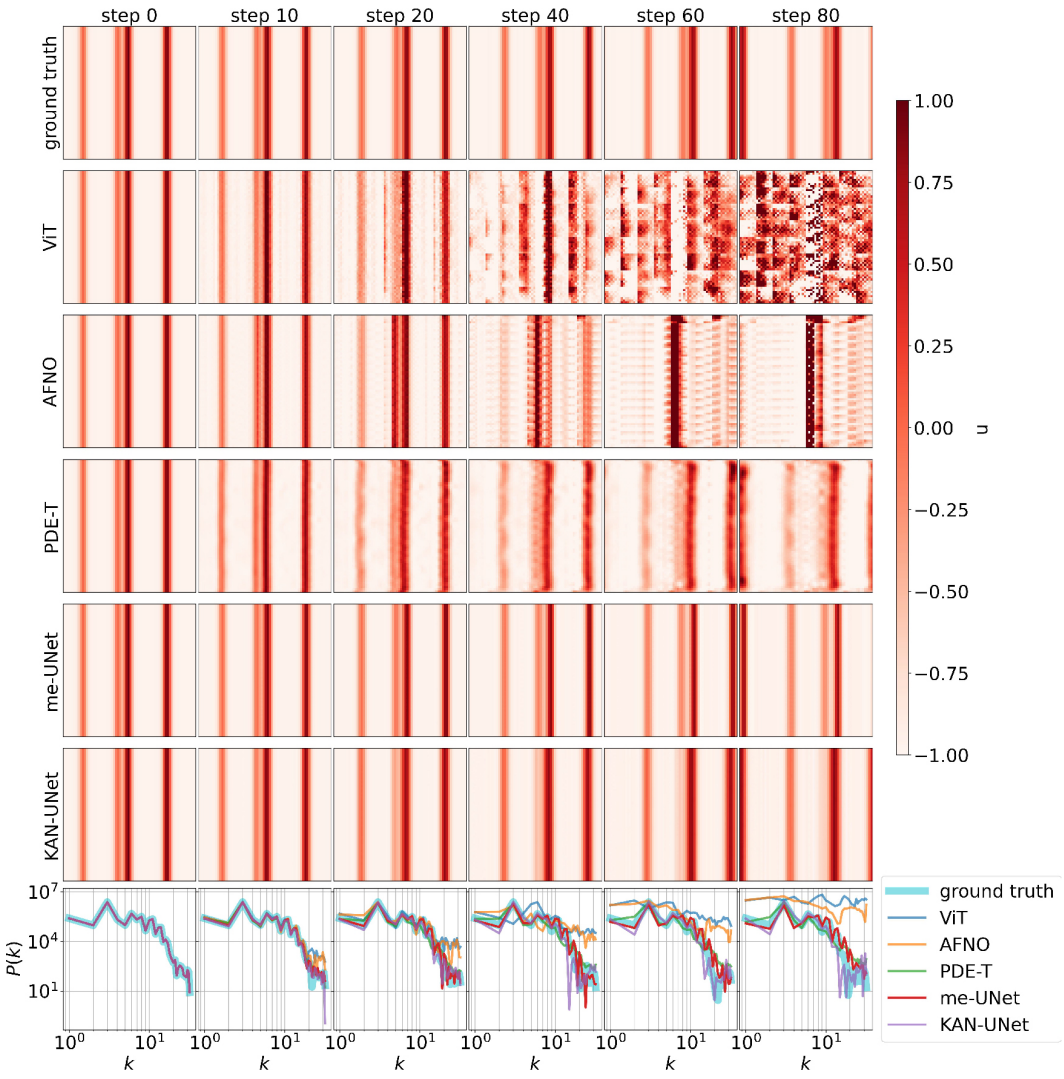

(a)

Figure 16: Visualization of the performance of the different neural networks on the DS-1 dataset.

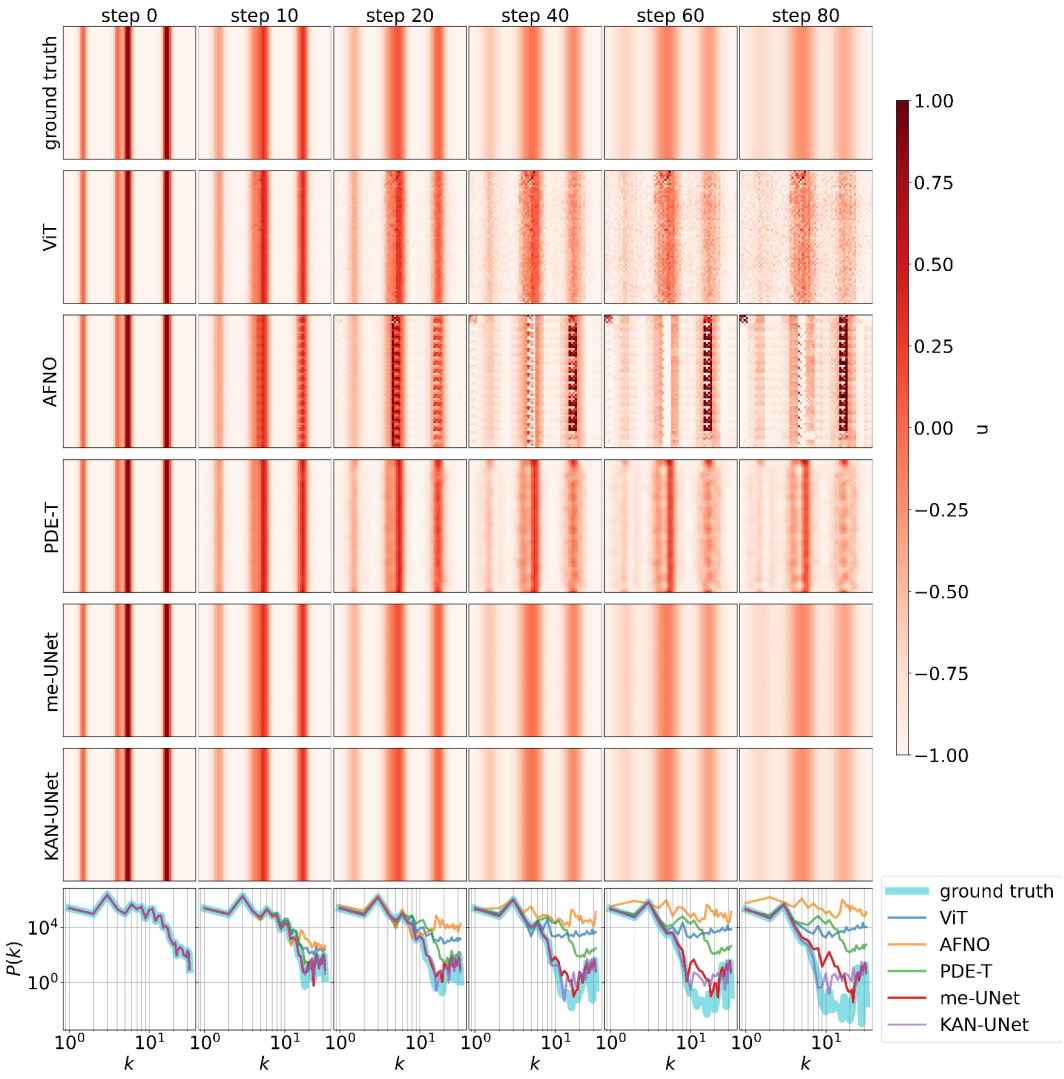

(a)

Figure 17: Visualization of the performance of the different neural networks on the DS-2 dataset.

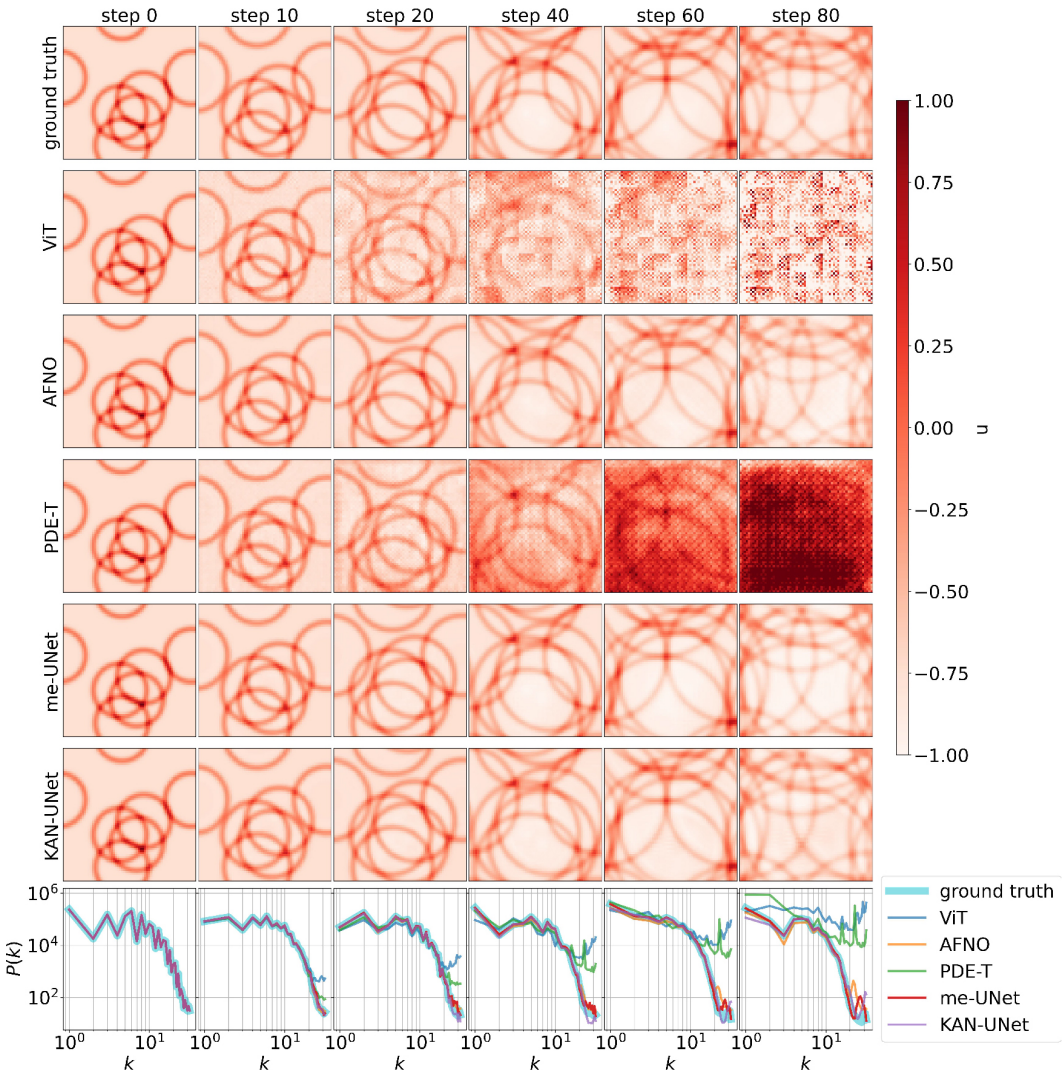

(a)

Figure 18: Visualization of the performance of the different neural networks on the DS-3a dataset.

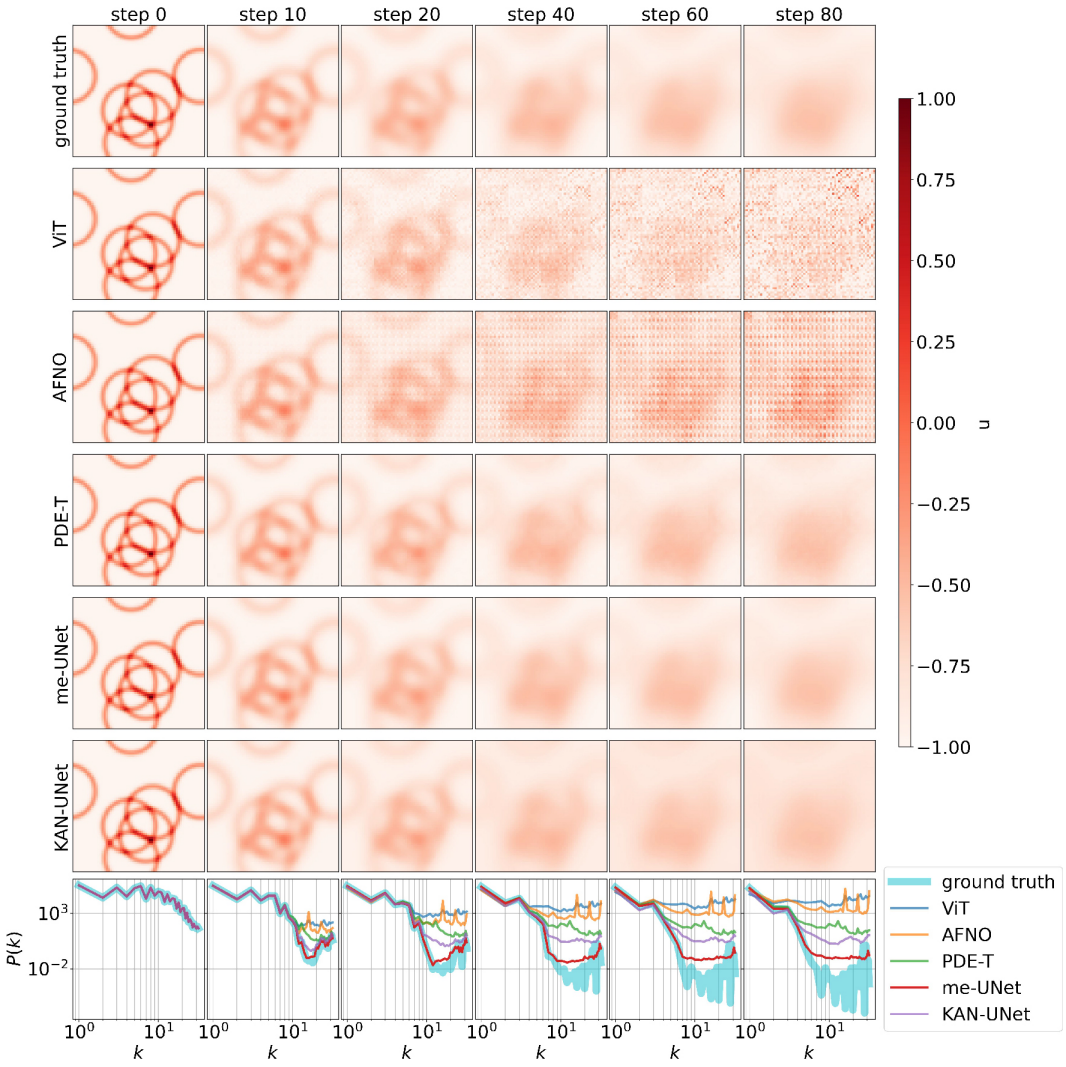

(a)

Figure 19: Visualization of the performance of the different neural networks on the DS-3b dataset.

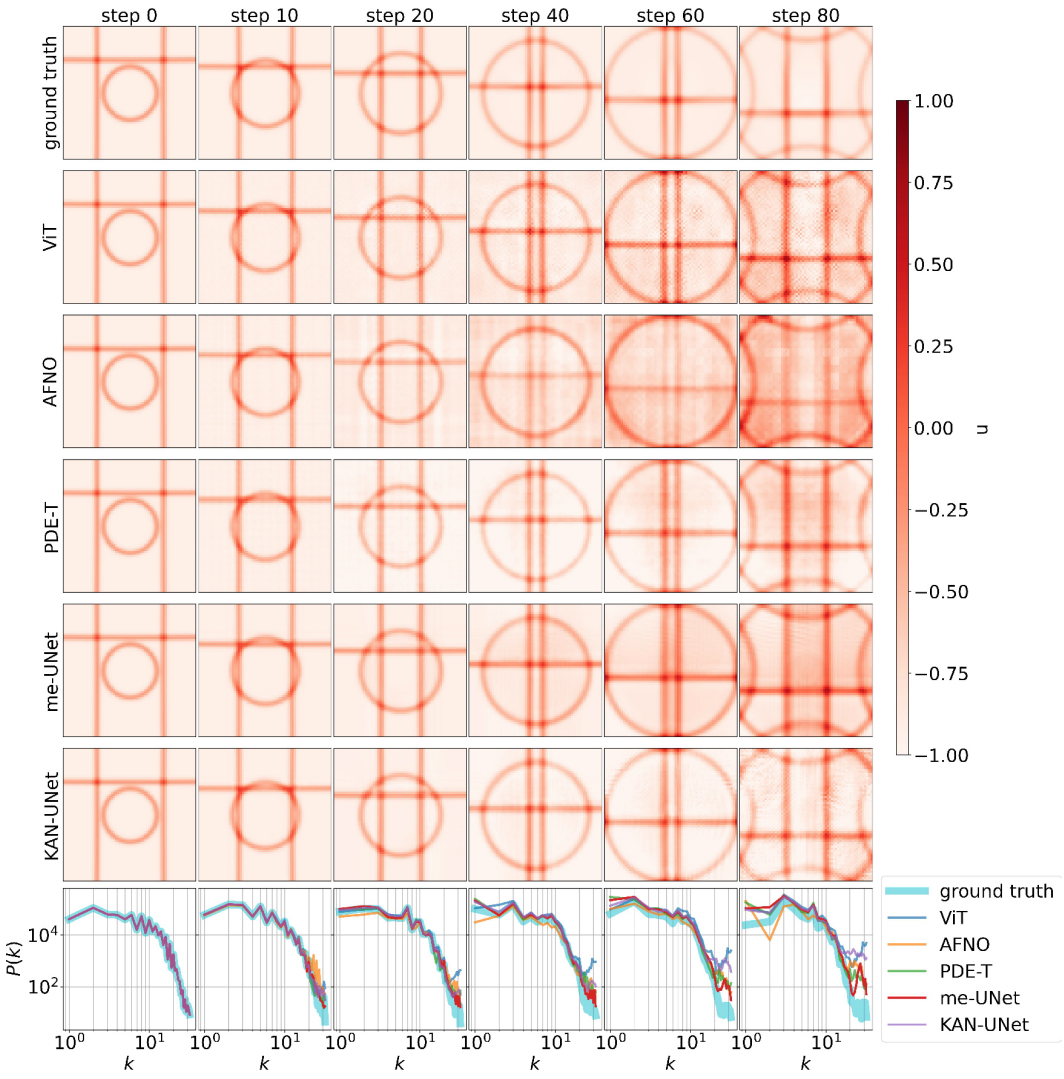

(a)

Figure 20: Performance of the different neural network architectures on the CDD dataset DS-4.

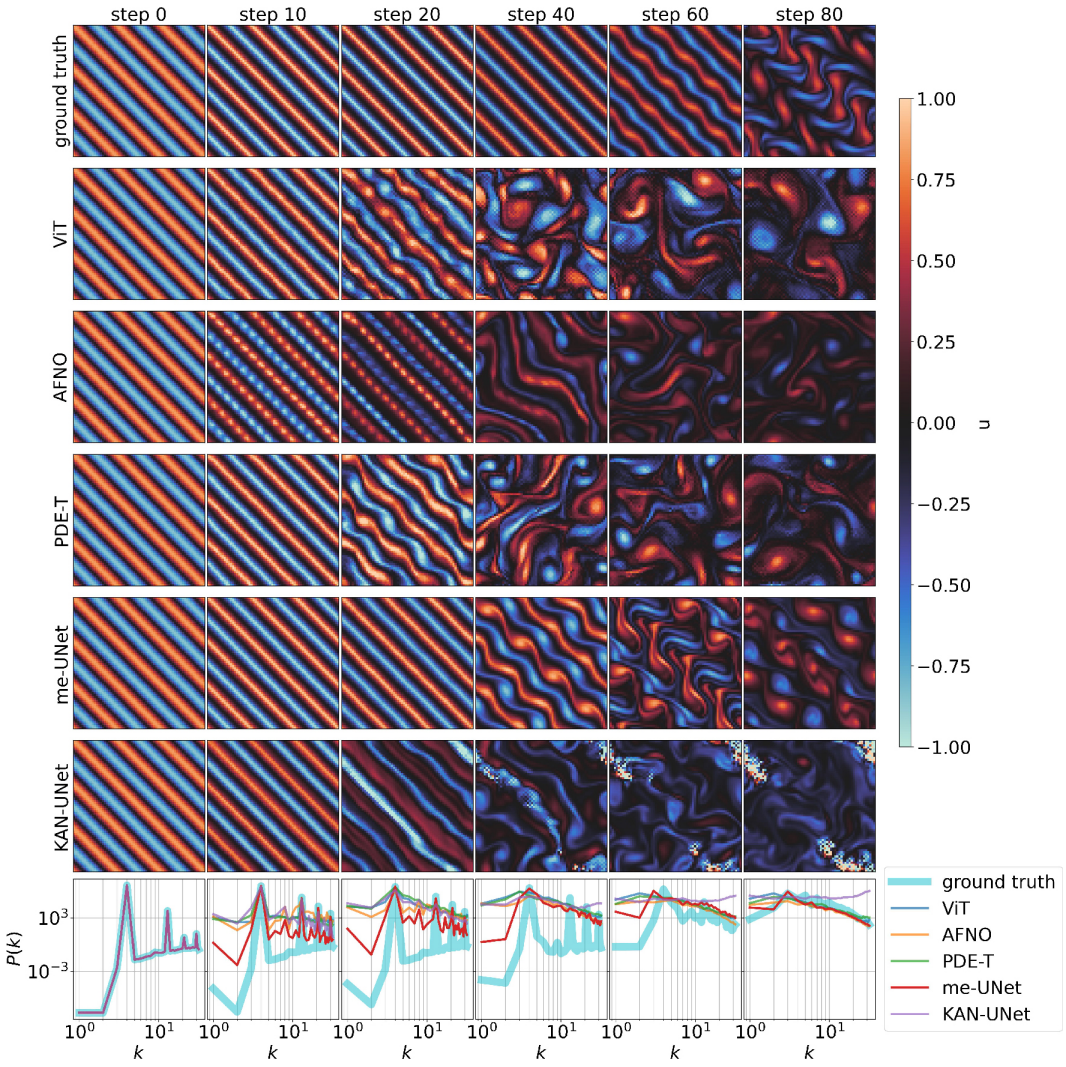

(a)

Figure 21: Visualization of the performance of the different neural networks on the DS-5 dataset.

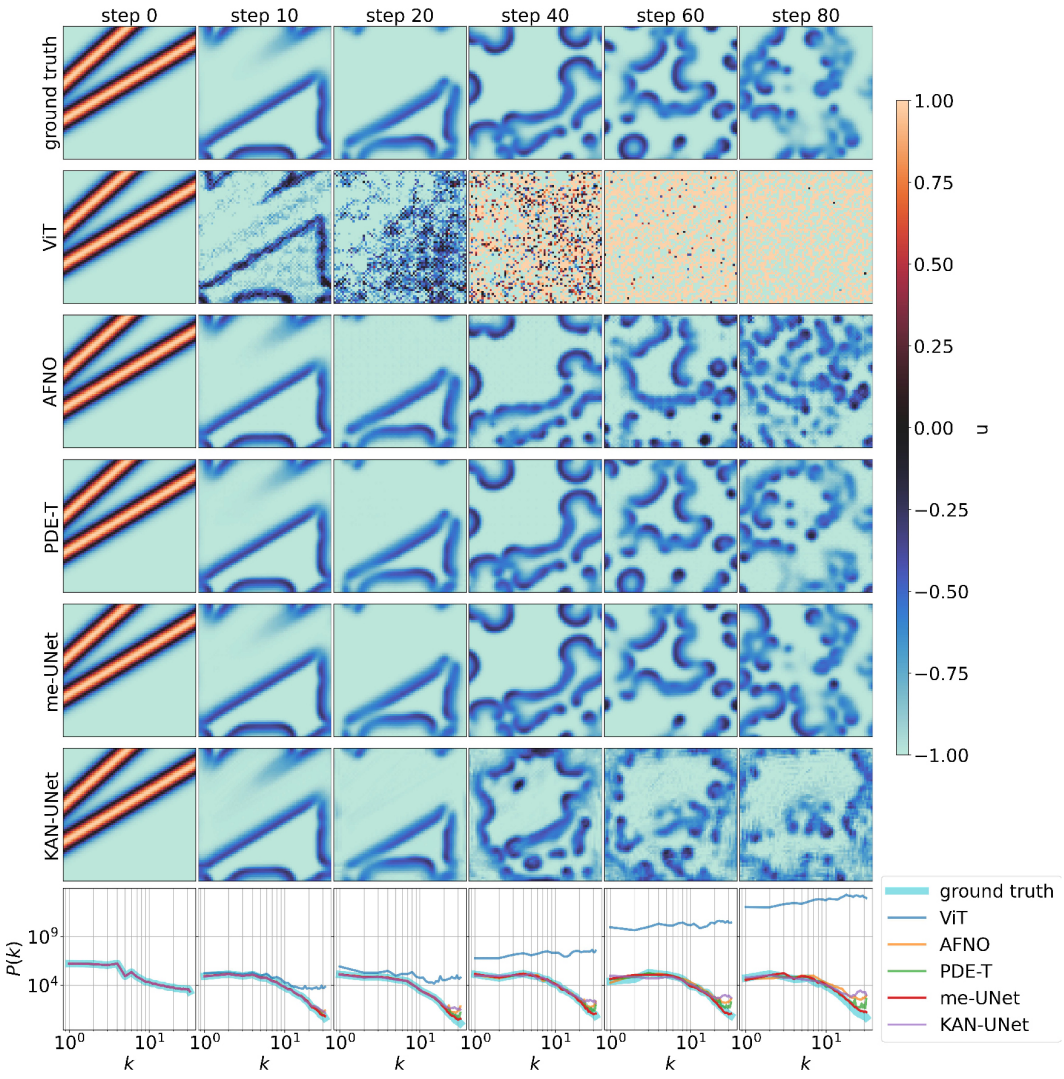

(a)

Figure 22: Visualization of the performance of the different neural networks on the DS-6b dataset.

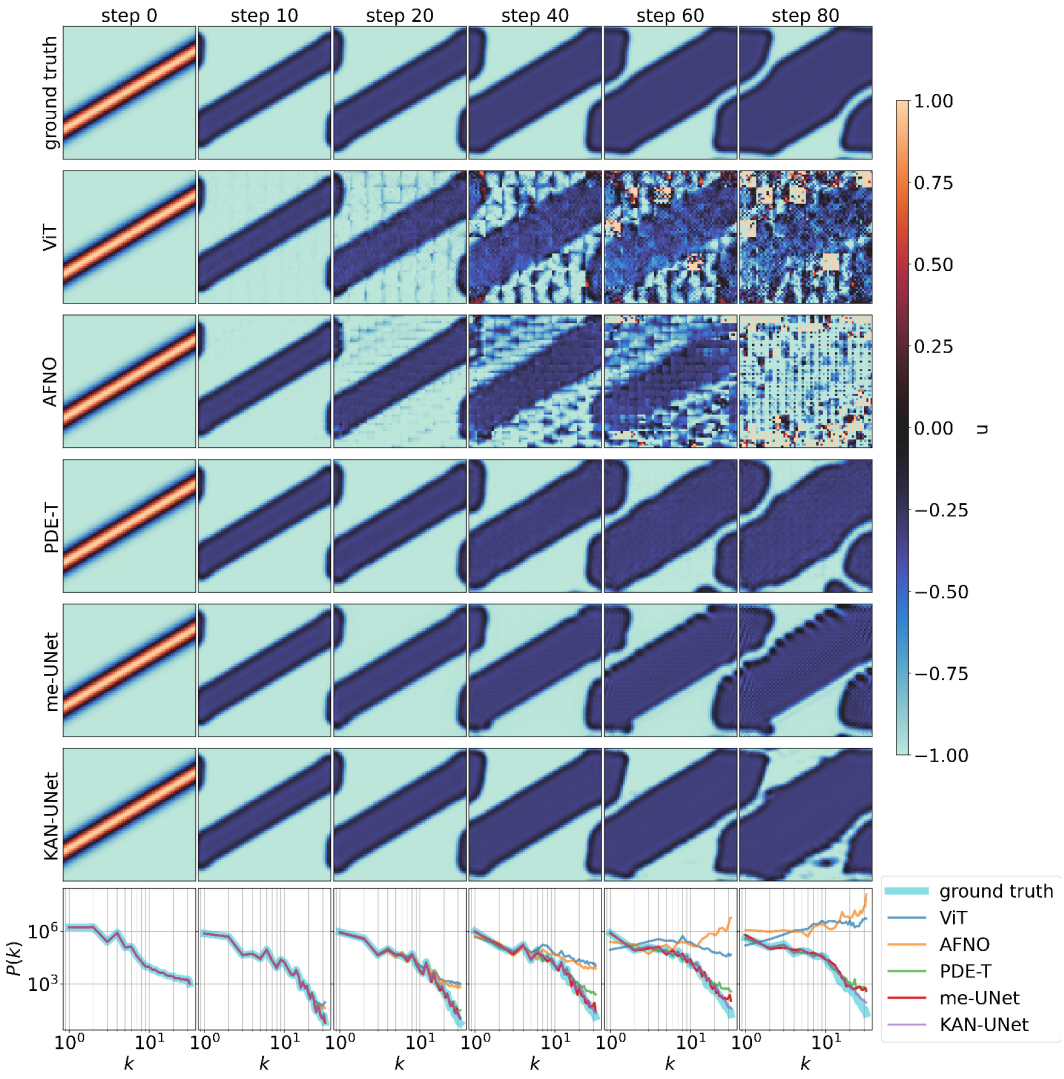

(a)

Figure 23: Visualization of the performance of the different neural networks on the DS-6c dataset.

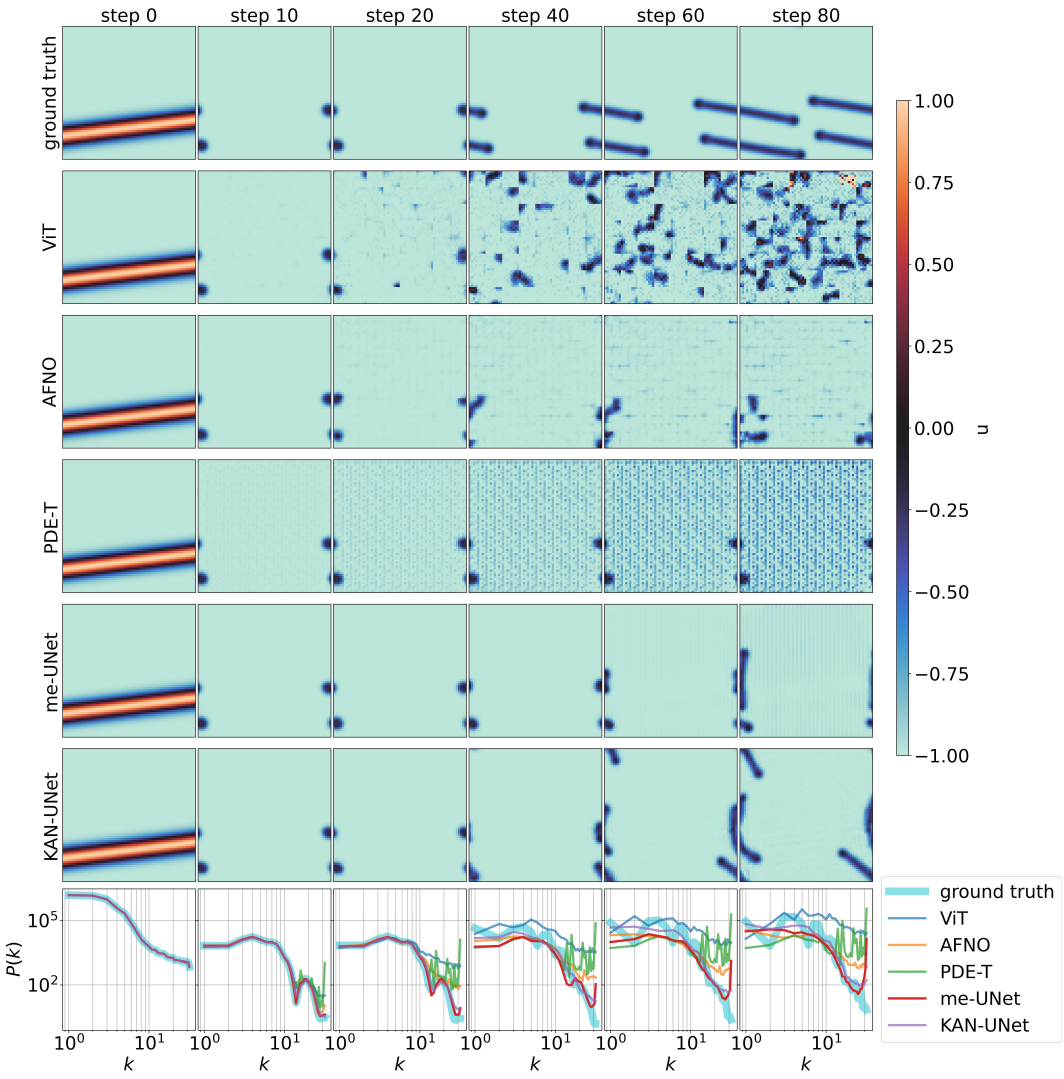

(a)

Figure 24: Visualization of the performance of the different neural networks on the DS-6d dataset.

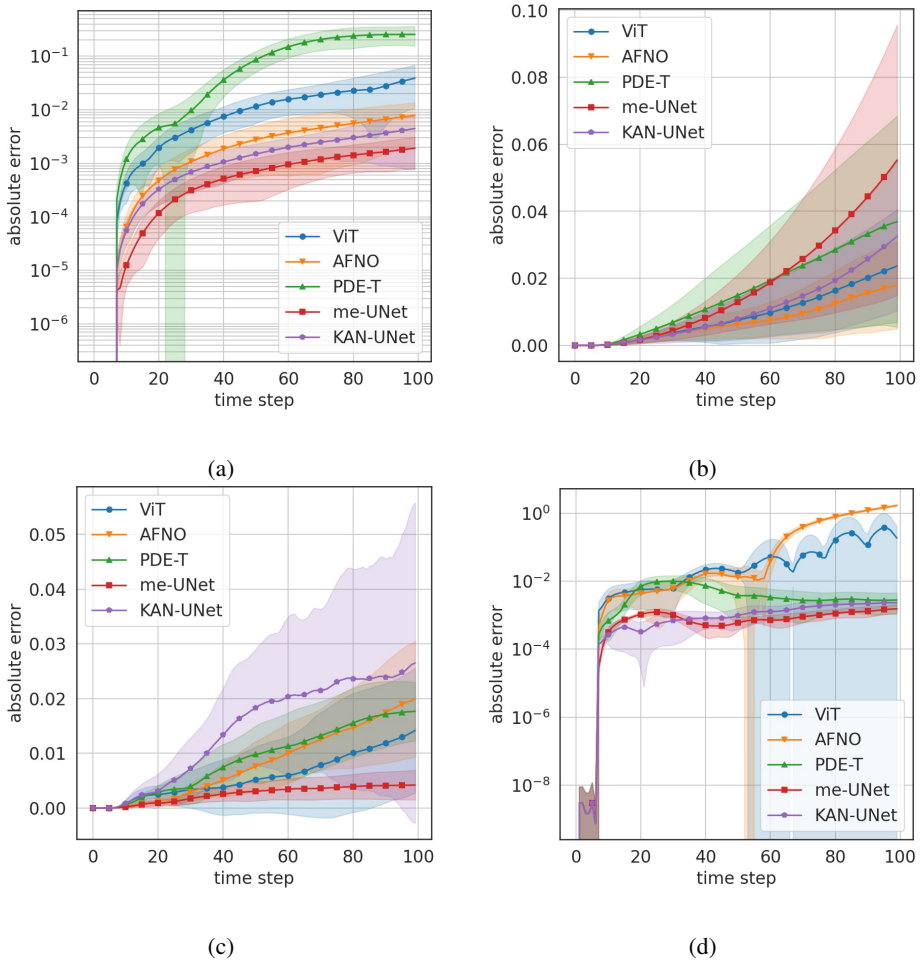

Figure 25: Normalized absolute error of physics-based metrics for (a) DS-3a, (b) DS-4, (c) DS-5, and (d) DS-6a.

C VISUALIZATION OF PHYSICS-BASED METRICS FOR OOD INITIAL CONDITIONS

In this section we show the corresponding physics-based metrics for the OOD initial-condition experiments described in section 3. Figure 26 displays spatial integrals of the monitored quantities for CDD and Gray–Scott rollouts under different OOD initial states. As in the in-distribution case, me-UNet tracks the reference integrals most closely over time, while several baselines exhibit noticeable drift, particularly for the more challenging line- and blob-type initial conditions.

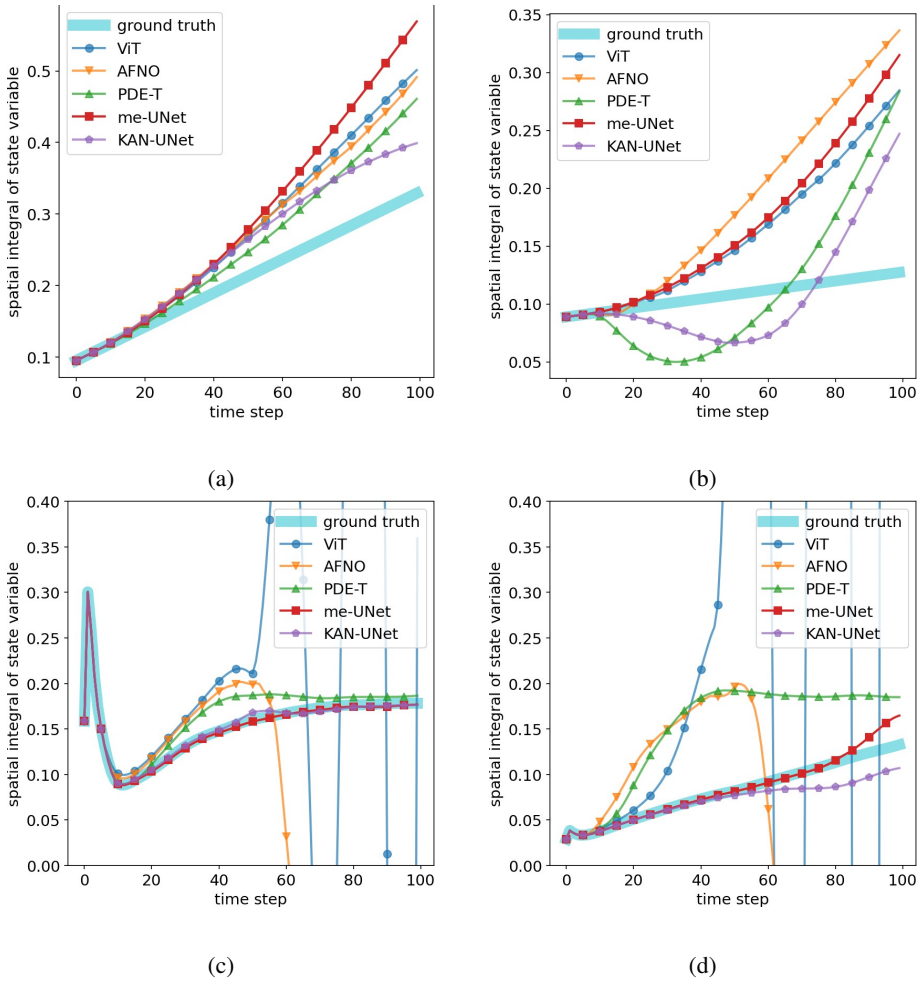

Figure 26: Spatial integrals of the monitored quantities for OOD rollouts on (a) DS-4 with initial few loops, (b) DS-4 with mixed lines and loops, (c) DS-6a with line-like initial conditions, and (d) DS-6a with blob-like initial conditions.